Most axonal mitochondria in cortical pyramidal neurons lack mitochondrial DNA and consume ATP

Yusuke Hirabayashi[1#*], Tommy L. Lewis Jr[2#*], Yudan Du[1], Daniel M. Virga[3,4,5], Aubrianna M. Decker[3], Giovanna Coceano[6], Jonatan Alvelid[6,7], Maëla A. Paul[5,8], Stevie Hamilton[4,5], Parker Kneis[2], Yasufumi Takahashi[9, 10], Jellert T. Gaublomme[3], Ilaria Testa[6], Franck Polleux[4,5*§]

[1] Department of Chemistry and Biotechnology, Graduate School of Engineering, The University of Tokyo; Tokyo, 113-8656, Japan
[2] Aging & Metabolism Program, Oklahoma Medical Research Foundation, Oklahoma City, OK 73104, USA
[3] Department of Biological Sciences, Columbia University; New York, NY, 10027, USA.
[4] Department of Neuroscience, Columbia University; New York, NY, 10027, USA.
[5] Mortimer B. Zuckerman Mind Brain Behavior Institute, Columbia University; New York, NY, 10027, USA.
[6] Department of Applied Physics and SciLifeLab, KTH Royal Institute of Technology, Stockholm, Sweden
[7] Department of Biophysical Imaging, Leibniz Institute of Photonic Technology, Jena, Germany
[8] Center for Interdisciplinary Research in Biology (CIRB), College de France, CNRS, INSERM, Université PSL; Paris, France
[9] Department of Electronics, Graduate School of Engineering, Nagoya University, 464-8603, Nagoya, Japan
[10] Nano Life Science Institute (WPI-NanoLSI), Kanazawa University, Kakuma-machi, Kanazawa, Ishikawa, 920–1192 Japan

# These authors contributed equally to this work.
[§] Lead author

* Co-corresponding authors:

Franck Polleux
Columbia University
Department of Neuroscience
Mortimer B. Zuckerman Mind Brain Behavior Institute
Jerome L. Greene Science Center
3227 Broadway
L-5-050, MC 9853
New York, NY 10027
USA
fp2304@columbia.edu

Yusuke Hirabayashi
hirabayashi@chembio.t.u-tokyo.ac.jp

Tommy L Lewis Jr
tommy-lewis@omrf.org

Abstract

In neurons of the mammalian central nervous system (CNS), axonal mitochondria are thought to be indispensable for supplying ATP during energy-consuming processes such as neurotransmitter release. Here, we demonstrate using multiple, independent, *in vitro* and *in vivo* approaches that the majority (~80-90%) of axonal mitochondria in cortical pyramidal neurons (CPNs), lack mitochondrial DNA (mtDNA). Using dynamic, optical imaging analysis of genetically encoded sensors for mitochondrial matrix ATP and pH, we demonstrate that in axons of CPNs, but not in their dendrites, mitochondrial complex V (ATP synthase) functions in a reverse way, consuming ATP and protruding H^+ out of the matrix to maintain mitochondrial membrane potential. Our results demonstrate that in mammalian CPNs, axonal mitochondria do not play a major role in ATP supply, despite playing other functions critical to regulating neurotransmission such as Ca^{2+} buffering.

Main Text

Mitochondria are often referred to as the 'powerhouse' of the cell because of their ability, through oxidative phosphorylation, to generate large amounts of ATP. The human brain is often considered the most energy consuming organ in our body representing only 2% of our body mass but consuming up to ~20% of glucose (*1*). In neurons of the CNS, mitochondria-dependent ATP synthesis through oxidative phosphorylation is thought to play a significant role in supporting key, energy-consuming, neuronal functions such as presynaptic neurotransmitter release along axons (*2-7*). However, several observations cast doubt on how critical axonal mitochondria are for ATP generation in mammalian CNS neurons: (1) only 50% of presynaptic boutons along axons of CPNs are associated with small (~1μm) mitochondria (*8-11*), (2) presynaptic release sites lacking mitochondria are characterized by higher neurotransmitter release probability than the presynaptic boutons associated with mitochondria (*9, 12*), and (3) blocking oxidative phosphorylation in mammalian neuronal culture has limited effects on presynaptic ATP concentration, even under extreme, non-physiological, levels of action potential-triggered stimulation of presynaptic release (*5, 13*). Interestingly, a recent proteomic study using synaptosomes isolated from glutamatergic cortical PNs reveal an enrichment in glycolytic proteins and a relative depletion in proteins involved in oxidative phosphorylation (*14*). Surprisingly, conditional deletion of mtDNA associated protein Twinkle has important consequences on astrocyte maintenance but relatively minor consequences on neuronal survival until 8 months despite significant loss of mtDNA in neurons, arguing that neurons can tolerate mtDNA loss significantly better than astrocytes in the CNS (*15*). Alternate sources of ATP

generation are available to neurons *in vivo*, such as glycolysis which is highly functional in axons (*1, 16-19*).

To tackle whether axonal mitochondria are indeed required for ATP production in this neuronal compartment, we first assessed the presence of mitochondrial DNA (mtDNA) in individual dendritic versus axonal mitochondria in developing and mature mouse CPNs *in vitro* and *in vivo*. Using multiple, independent *in vitro* and *in vivo* approaches such as (1) immunofluorescence detection of mtDNA and visualization of mtDNA-associated proteins such as Twinkle and TFAM, (2) single molecule DNA-FISH for mtDNA, as well as (3) quantitative PCR from single axonal mitochondria, our results demonstrate that mtDNA is completely undetectable in ~80-90% of axonal mitochondria. Furthermore, live imaging analysis using mitochondrial matrix-targeted, genetically encoded sensors for ATP (mt-iATPSnFR1.0) as well as pH (mt-SypHer) demonstrate that in axonal, but not in dendritic mitochondria, complex V (ATP synthase) functions in a reverse way, consuming ATP and protruding H^+ out of the matrix to maintain mitochondrial membrane potential. Together, our results suggest a major revision of the role of axonal mitochondria, at least in mammalian cortical pyramidal neurons, since they do not seem to play a major role in ATP generation, despite playing other critical functions at presynaptic release sites such as Ca^{2+} buffering.

Most axonal mitochondria lack mtDNA and mtDNA-associated proteins in CPNs *in vitro* and *in vivo.*

We used *ex utero* electroporation (EUE), performed at E15 to target progenitors generating layer 2/3 CPNs, to express the fluorescently tagged mtDNA-associated protein Twinkle and an outer mitochondrial membrane (OMM) targeted mCherry (mCherry-ActA) (**Fig. 1**), followed by dissociation and maintenance in high-density cultures for 5-15 days *in vitro* (DIV). Upon fixation, we coupled fluorescent detection of Twinkle-Venus and mCherry-ActA with an antibody-based detection of DNA (*20*)(**Fig. 1A**). We also labeled mitochondria with outer mitochondrial membrane (OMM) targeted mCherry (mCherry-ActA). Quantification of the fraction of mitochondria positive for either or both DNA immunofluorescence and Twinkle-Venus gives consistent results and reveals striking differences between axons and dendrites (**Fig. 1B**): in dendrites the fraction of mitochondria containing mtDNA is ~70% but in axons this fraction goes down to ~10-20%. This low fraction of Twinkle+ axonal mitochondria is slightly but significantly higher in immature CPNs in vitro (~20% at 5DIV) and decreases progressively with neuronal maturation down to ~10% at 10-15DIV (**Fig. 1C**).

Using *in utero* electroporation (IUE) at E15 of neural progenitors generating layer 2/3 CPNs progenitors and examining mature neurons at P27, we confirmed that a low fraction of Twinkle+ mitochondria along the distal portion of the axon (**Fig. 1D**). Interestingly, we observed that in the portion of axon most proximal to the soma (<20µm), corresponding to the axon initial segment (AIS), the fraction of Twinkle+ mitochondria reaches approximately 50%, while the portion of the axon more distal to the soma (>20µm) has a significantly lower fraction (~20%; **Fig. 1D-E**). We obtained the same results in layer 2/3 CPNs *in vivo* using a different nucleoid/mtDNA-associated protein (TFAM-mCherry) expressed by IUE, with less than 20% of axonal mitochondria being TFAM+, whereas ~60% of dendritic mitochondria are TFAM+ (**Supplementary Fig. 1**).

In mammalian cells, mitochondria nucleoids display a uniform small size on the order of a hundred nanometers (*21*) and contain both mtDNA and its associated proteins such as TFAM and Twinkle (*22*). In order to exclude the possibility that the low fraction of mtDNA+ mitochondria we observed in axons of CPNs *in vitro* and *in vivo* could be due to our inability to detect them with diffraction-limited confocal microscopy, we used customized Stimulated Emission Depletion (STED) microscopy, a super-resolution microscopy technique with 80 nm axial and 40 nm lateral resolution. We imaged rat hippocampal neurons maintained for 7-9DIV or 14-16DIV (**Fig. 2A-E**) stained with the dendritic marker Map2 (cyan in **Fig. 2A** and **C**) or and AIS marker, Neurofascin (NF; AIS in **Fig. 2D-E**), an anti-DNA antibody (yellow in **Fig. 2A-C**) or anti-TFAM antibody (yellow in **Fig. 2D-E**) to label nucleoids and an antibody against the outer mitochondrial membrane protein (OMM) Tom20 (magenta in **Fig. 2A-C**) or OMP25 localization peptide (magenta in **Fig. 2 D-E**) to label the OMM. Both in Map2+ dendritic segments (white arrows in **Fig. 2B-C**) and in the AIS (**Fig. 2D-E**), the use of STED super-resolution microscopy (**Fig. 2B&D**) drastically improved resolution of individual mtDNA+ or TFAM+ nucleoids compared to confocal microscopy (**Fig. 2C&E**). This improvement in spatial resolution allowed the quantification of the number of nucleoids in axonal and dendritic mitochondria (**Fig. 2F**) as well as the correlation of mitochondria size with nucleoid number per mitochondria in axons (**Fig. 2G**). These results show that the majority (56%) of axonal mitochondria contain zero nucleoids detectable by STED microscopy whereas only 35% of dendritic mitochondria contain zero nucleoids (**Fig. 2F**). In the axon, we observe a relationship between mitochondria size and nucleoid number (**Fig. 2G**). 2D-STED volumetric imaging of non-nuclear DNA but in the soma of a hippocampal neuron (**Fig. 2H**) reveals numerous nucleoids dispersed over the soma and accumulating in dendritic mitochondria emerging from the cell body (arrows in **Fig. 2H**) with very

few detected towards and into the AIS (labeled by NF, not shown). Importantly, quantification of the fraction of nucleoid-containing mitochondria along the length of the axons of hippocampal neurons at 7-9DIV (**Fig. 2J**) shows that ~50-60% of axonal mitochondria are TFAM-negative, a percentage that increases significantly (to ~80-90%) of nucleoid-negative mitochondria in the distal portion (>80µm from soma) of the axon at 14-16DIV (**Fig. 2K**).

A low fraction of axonal mitochondria contains mtDNA detected using DNA-FISH.

One potential reason for detection of such a low fraction of nucleoid+ mitochondria in axons of cortical and hippocampal pyramidal neurons *in vitro* and *in vivo* could be the relatively poor sensitivity of antibody-based detection of mtDNA or plasmid-based expression of mtDNA-associated proteins such as TFAM or Twinkle. We therefore implemented the use of independent endogenous mtDNA detection methods. First, we implemented DNA-fluorescent *in situ* hybridization (DNA-FISH) using probes detecting two mitochondrial DNA encoded genes: Cytochrome b (Cytb) and Cytochrome oxidase 1 (Cox1). DNA-FISH for mtDNA was applied to mature cortical neuron cultures at 21DIV where mt-YFP (matrix-targeted YFP) was sparsely expressed in layer 2/3 CPNs using EUE at E15 (**Fig. 3A-B**). Quantification reveals that only ~4% of axonal mitochondria are labeled with either Cytb and/or Cox1 probes whereas ~97% of dendritic mitochondria are positive for mtDNA probes detecting Cytb and/or Cox1 (**Fig. 3C-D**). As previously shown (*10*), we confirmed that in these culture conditions, dendritic mitochondria of CPNs are large, elongated and fused, whereas axonal mitochondria are small, at an average of approximately 1µm in length (**Fig. 3E**).

A low fraction of axonal mitochondria contains mtDNA detected using quantitative PCR from single mitochondria isolated by Scanning Ion Conductance Microscopy (SICM)

We also developed an independent way to detect mtDNA in single mitochondria that does not rely on imaging, by modifying and implementing Scanning Ion Conductance Microscopy (SICM)(*23*). Briefly, single mitochondria were extracted via an epifluorescence microscope equipped with a nanopipette that contains an internal Ag/AgCl electrode inside for monitoring the ionic current between the electrode and cell surface. Femto- to picoliters of liquid can be captured into the pipette by transiently increasing the potential on the electrode (**Fig. 3F**) (*24, 25*). We isolated individual mitochondria using SICM in CPNs expressing Twinkle-mRuby3 and maintained in culture with a physiological range of glucose concentrations (5 - 10 mM) for 7-9DIV. A mitochondrial matrix-targeted YFP (mt-YFP) was expressed

to visualize all the mitochondria in the culture. This approach allows visually guided capture of individual Twinkle+ or Twinkle- mitochondria in axons or dendrites (**Fig. 3G-I, Supplementary Movie 1)**. Upon isolation of single axonal or dendritic mitochondria, we performed calibrated (**Fig. 3J**) quantitative PCR using dual-labeled probes to measure the presence of mtDNA in a highly specific and efficient manner (**Fig. 3K**). This analysis confirms that only a small (~10%) fraction of axonal mitochondria contains qPCR-detectable mtDNA, whereas the vast majority of dendritic mitochondria contain multiple mtDNA copies (**Fig. 3K, Supplementary Figure 2**).

Taken together, our results identify a fundamental difference between axonal and dendritic mitochondria regarding mtDNA content: in CPNs, dendritic mitochondria form a dense, fused, elongated network containing numerous mtDNA+ nucleoid whereas the vast majority of axonal mitochondria are small (~1μm in length) and do not contain mtDNA. We previously demonstrated that the striking degree of compartmentalization of mitochondrial structure between axons and dendrites of CPNs observed *in vivo* (*26*) is controlled by a significant difference in the fusion/fission balance, with MFF-dependent fission being much more prevalent in axons (*10*). However, our new results regarding the striking difference in mtDNA content between axonal and dendritic mitochondria raise an important question: are these structural differences reflecting a deep functional divergence? In eukaryotic cells, the 16.5 kB long mtDNA contains 37 genes, 13 of which encode proteins, 22 encode tRNAs and 2 encode ribosomal RNAs used for mitochondrial translation. The 13 protein-coding genes contained in the mitochondrial genome encode several key proteins contained in the large complexes composing the electron transport chain such as the ND1-6 subunits of Complex I (NADH dehydrogenase), Cytochrome b (Cytb; Complex III) and Cytochrome c oxidase (Complex IV) and two subunits of the ATP synthase (Complex V). Therefore, one would hypothesize that axonal mitochondria lacking mtDNA would have a poorly effective ETC and therefore relatively low capacity for oxidative phosphorylation and ATP synthesis.

Most axonal mitochondria enter the axon from the soma lacking mtDNA.

What are the cellular mechanisms leading to such a low fraction of axonal mitochondria containing mtDNA? We envisioned two potential mechanisms: (1) Since recent work demonstrated that in mammalian cell lines, mtDNA replication is coupled with mitochondrial fission to ensure that both 'daughter' mitochondria both contain mtDNA (*27-29*), we hypothesize that the high levels of MFF-dependent fission characterizing mitochondria of CPNs axons (*10*) might be non-replicative, progressively diluting the fraction of mitochondria containing mtDNA with each round of fission. (2) Not incompatible

with the first model, a large fraction of mitochondria entering the axon from the soma could already be lacking mtDNA.

We tested the first model, i.e. if a high rate of fission is required for the lack of mtDNA+ mitochondria in axons of CPNs, by blocking mitochondrial fission using shRNA-mediated knockdown of mitochondrial fission factor (Mff) (*10*). We performed *ex utero* electroporation (EUE) at E15.5 with plasmids encoding matrix targeted mScarlet (mt-mScarlet) and either a control shRNA or the previously validated Mff shRNA (*10*) followed by *in vitro* dissociated culture. At 21DIV, mature CPNs cultures were fixed and stained for mScarlet and endogenous DNA to visualize mtDNA in axonal mitochondria (**Supplementary Figure 3A-B**). Interestingly, we observed no significant change in the percentage of axonal mitochondria containing mtDNA arguing that mitochondrial fission in not a major contributor to the lack of mtDNA in axonal mitochondria of CPNs (**Supplementary Figure 3C**).

To test the second model i.e. to determine whether axonal mitochondria enter the axon already devoid of a nucleoid/mtDNA, we performed timelapse imaging of axonal mitochondria in CPNs expressing OMM targeted-mCherry (mCherry-ActA) and Twinkle-Venus to label mtDNA-associated nucleoids (**Supplementary Figure 3D-F**). Following 15 minutes of live imaging, we observed between 1 to 8 mitochondria entering the axon from the cell body (**Supplementary Figure 3F**). Surprisingly, in ~75% (13/17) of the axons imaged, none of the axonal mitochondria entering the axon during the 15 minutes period of imaging were positive for Twinkle-Venus (**Supplementary Figure 3F**). Of the 17 axons imaged, we observed only 5.6% (4/71) of axonal mitochondria entering the axon to be Twinkle-Venus+ (**Supplementary Figure 3G**). This strongly suggests that the majority of somatic fission events generating the small (~1μm-long) mitochondria selected to enter the axon already lack mtDNA.

ATP synthase (Complex V) in axonal mitochondria functions in reverse-mode extruding H^+ and consuming ATP to maintain mitochondrial membrane potential.

In most axonal mitochondria lacking mtDNA, the oxidative phosphorylation complexes mediating electron transport and H^+ extrusion across the inner mitochondrial membrane (IMM) should have strongly reduced efficiency. To determine whether axonal and dendritic mitochondria have distinct functional properties, we first tested whether mitochondrial matrix pH, i.e. H^+ concentration dynamics, differs in mitochondria found in these two compartments. Thus, we performed EUE at E15.5 to express a plasmid encoding a matrix targeted, fluorescent pH reporter (mt-SypHer; (*30*)) and a non-pH sensitive matrix targeted HA-mCherry to assess basal matrix pH in axonal and dendritic mitochondria of layer 2/3 CPNs

maintained in culture. Using live confocal microscopy, single dendritic and axonal segments were imaged from the same CPN allowing paired comparison of the mt-SypHer/mCherry ratio of axonal and dendritic mitochondria (**Fig. 4A**). Both at the individual mitochondrion level (**Fig. 4B**), and when averaged throughout a segment (**Fig. 4C**), axonal mitochondria consistently display a significantly higher SypHer/mCherry ratio, indicative of a more basic pH (lower H^+ concentration) in the matrix of axonal mitochondria, compared to dendritic mitochondria. To determine whether this more basic matrix pH is the result of altered H^+ flux by the ETC of axonal mitochondria, we treated CPN cultures expressing mt-SypHer and labeled with a membrane potential dye, tetramethylrhodamine (TMRM; 20 nM loading, 5 nM during imaging), with either a complex III (Antimycin A – 1.25 μM) or complex V (Oligomycin - 1.25 μM) inhibitor and measured variations in axonal mitochondria matrix pH and membrane potential (**Fig. 4D**).

As expected with mild complex III inhibition, the mitochondrial matrix acidified significantly (decreased fluorescence of mt-SypHer, i.e. increased [H^+] in mitochondrial matrix; (*30*)) and mitochondrial membrane potential (TMRM) drops rapidly (**Fig. 4E-H**). This suggests that Complex III is functioning, at least to some extent, in axonal mitochondria, contributing to some H^+ extrusion outside the matrix. However, with Oligomycin treatment which blocks complex V (ATP synthase) inhibition, instead of the expected de-acidification (reduction in matrix [H^+]) and hyperpolarization of the membrane potential, we observed again that the matrix acidifies and membrane potential drops (**Fig. 4E-H**). This strongly argues that in axonal mitochondria, complex V is working in reverse mode protruding H^+ out of the matrix, and that axonal mitochondria may in fact be consuming, instead of producing, ATP, and thereby participating to the maintenance of mitochondrial membrane potential.

To test this possibility, we measured mitochondrial matrix ATP dynamics following inhibition of the adenine nucleotide translocase (ANT) with bongkrekic acid (BKA- 50 μM) (*31*). We induced expression of a plasmid encoding a matrix targeted iATPSnFR1.0 (mt-iATPSnFR;(*32*)) fused with mScarlet using EUE at E15.5, then at 17DIV, we performed live imaging before and after BKA application (**Fig. 4I**). Since iATPSnFR is pH sensitive, we first confirmed that over the time frame of the imaging experiment matrix pH is not significantly altered by BKA addition by imaging over the soma (**Supplementary Fig. 4**). We then imaged mt-iATPSnFR dynamics in both dendritic and axonal mitochondria upon addition of BKA, and observed an increase in the mt-iATPSnFR signal of dendritic mitochondria, indicative of ATP accumulation in the matrix following ANT inhibition (**Fig. 4J-K**). Instead in axonal mitochondria, mt-

iATPSnFR decreased over time, suggesting that ATP is consumed in the matrix of axonal mitochondria at resting state (**Fig. 4J-K**).

Discussion

Mitochondria were recently shown to display distinct patterns of dynamics and morphology in dendrites and axons (*10, 33*), but the functional correlates of these structural observations, if any, at the level of neuronal metabolism remained unknown. Here we show that axonal mitochondria do not only display small size but also are mostly devoid of nucleoids and therefore mostly inactive ETC. Taken together with previously published results demonstrating the profound differences in mitochondria structure between axons and dendrites in mammalian long-projecting cortical pyramidal neurons (*10, 26, 34*), the results obtained in this study demonstrate that these striking structural differences have a functional correlate. In dendrites of CPNs, mitochondria are elongated and highly fused, with their network occupying a large fraction of the dendritic arbor and are highly metabolically active generating ATP while containing numerous mtDNA-nucleoids. In contrast, axonal mitochondria in the same neurons are small (~1µm long), mostly lacking mtDNA, and instead of generating ATP are consuming ATP through the reverse action of their ATP synthase (Complex V) to maintain a physiological membrane potential range. We speculate the reason Complex V consumes ATP and protrudes H^+ outside the matrix at steady state is due to the fact that some of the key functions of presynaptic axonal mitochondria, such as MCU-dependent Ca^{2+} import, require mitochondrial membrane potential to be maintained within a specific 'physiological' range (*35*). The surprising model emerging from our results is that the main source of ATP in axons of mammalian CPNs could be intrinsic glycolysis, whereas mitochondria in the dendritic compartment are fully competent to generate ATP through oxidative phosphorylation. What could be the biological adaptation of such a drastic difference between the mtDNA content and ATP generation capacity between axonal and dendritic mitochondria in mammalian CPNs? We speculate four potential models to explain this drastic level of compartmentalization of mitochondrial function: (1) the cytoplasmic volume at individual presynaptic bouton is extremely small (in the order of hundreds of cubic nanometers) and therefore, in such extremely small volumes, the accumulation of mitochondria-derived reactive-oxygen species (ROS), a byproduct of highly functional ETC, could be damaging to protein complexes involved in neurotransmission; (2) mitochondria with highly functioning electron transport chain and high levels of oxidative phosphorylation have been proposed to reach temperatures approaching 50ºC (*36, 37*). Since axonal mitochondria are located just a few hundreds of nanometers from the active zone at presynaptic

boutons, where SNARE-mediated presynaptic vesicles are docked near the plasma membrane, and SNARE-mediated exocytosis is highly temperature-dependent (*38*), we speculate that axonal mitochondria with defective or poorly functioning oxidative phosphorylation characterizing CPNs described in this study might not generate high temperatures and therefore not interfere with SNARE-mediated presynaptic vesicle fusion; (3) Axonal mitochondria are more inclined towards electron transport chain-independent anabolic functions, such as amino acid biosynthesis (*39, 40*) including glutamate generation, the primary excitatory neurotransmitter used by CPNs and/or to fuel local protein synthesis which is prevalent, and often associated with mitochondria, not only in dendrites (*5, 14*) but also in distal portions of the axon in neurons (*41, 42*); (4) recent work suggests that mtDNA-mediated activation of the cGAS-STING pathway triggers low grade inflammation and senescence-associated secretory phenotypes found in aging and neurodegeneration (*43, 44*). Therefore, limiting the abundance of mtDNA along CNS axons might have been selected during evolution to limit cGAS-STING engagement during the lifetime of long-lived vertebrates in a neuronal compartment where mitophagy is prevalent (*45, 46*).

Future investigations will determine if the results obtained in this study on long-range projecting, glutamatergic mouse CPNs can be generalized or not to other subtypes of neurons in the mammalian CNS. For example, in the neocortex, subtypes of GABAergic interneurons such as Parvalbumin (PV)+ fast-spiking basket cell interneurons have been hypothesized to have higher metabolic demand due to their unusually high ability to spike action potentials at very high frequency (>100Hz for seconds long burst) (*47*). In fact, a recent proteomic study performed on synaptosomes isolated from genetically labeled neurons including from PV+ interneurons suggested a significant enrichment of proteins involved in oxidative phosphorylation and a relative depletion of glycolytic enzymes, which is the opposite of synaptosomes isolated from glutamatergic CPNs (*14*). Another neuronal subtype with high metabolic load and high levels of activity are dopaminergic neurons in the substantia nigra pars compacta (SNc) which preferentially degenerate in Parkinson's disease and are highly vulnerable to oxidative stress and mitochondrial dysfunction (*48*). It will be important to explore if axonal or presynaptic mitochondria of PV+ interneurons or SNc dopaminergic neurons diverge from those found in CPNs and have a higher fraction of mtDNA+ mitochondria and higher oxidative phosphorylation capacity which could render these neurons selectively vulnerable to mitochondrial insults.

References

1. M. Belanger, I. Allaman, P. J. Magistretti, Brain energy metabolism: focus on astrocyte-neuron metabolic cooperation. *Cell Metab* **14**, 724-738 (2011).
2. M. J. Devine, J. T. Kittler, Mitochondria at the neuronal presynapse in health and disease. *Nat Rev Neurosci* **19**, 63-80 (2018).
3. J. J. Harris, R. Jolivet, D. Attwell, Synaptic energy use and supply. *Neuron* **75**, 762-777 (2012).
4. K. Mann, S. Deny, S. Ganguli, T. R. Clandinin, Coupling of activity, metabolism and behaviour across the Drosophila brain. *Nature* **593**, 244-248 (2021).
5. V. Rangaraju, N. Calloway, T. A. Ryan, Activity-driven local ATP synthesis is required for synaptic function. *Cell* **156**, 825-835 (2014).
6. S. Li, Z. H. Sheng, Energy matters: presynaptic metabolism and the maintenance of synaptic transmission. *Nat Rev Neurosci* **23**, 4-22 (2022).
7. P. Verstreken *et al.*, Synaptic mitochondria are critical for mobilization of reserve pool vesicles at Drosophila neuromuscular junctions. *Neuron* **47**, 365-378 (2005).
8. J. Courchet *et al.*, Terminal axon branching is regulated by the LKB1-NUAK1 kinase pathway via presynaptic mitochondrial capture. *Cell* **153**, 1510-1525 (2013).
9. S. K. Kwon *et al.*, LKB1 Regulates Mitochondria-Dependent Presynaptic Calcium Clearance and Neurotransmitter Release Properties at Excitatory Synapses along Cortical Axons. *PLoS Biol* **14**, e1002516 (2016).
10. T. L. Lewis, Jr., S. K. Kwon, A. Lee, R. Shaw, F. Polleux, MFF-dependent mitochondrial fission regulates presynaptic release and axon branching by limiting axonal mitochondria size. *Nat Commun* **9**, 5008 (2018).
11. H. L. Smith *et al.*, Mitochondrial support of persistent presynaptic vesicle mobilization with age-dependent synaptic growth after LTP. *Elife* **5**, (2016).
12. V. Vaccaro, M. J. Devine, N. F. Higgs, J. T. Kittler, Miro1-dependent mitochondrial positioning drives the rescaling of presynaptic Ca2+ signals during homeostatic plasticity. *EMBO Rep* **18**, 231-240 (2017).
13. D. Pathak *et al.*, The role of mitochondrially derived ATP in synaptic vesicle recycling. *J Biol Chem* **290**, 22325-22336 (2015).
14. M. van Oostrum *et al.*, The proteomic landscape of synaptic diversity across brain regions and cell types. *Cell* **186**, 5411-5427 e5423 (2023).
15. O. Ignatenko *et al.*, Loss of mtDNA activates astrocytes and leads to spongiotic encephalopathy. *Nat Commun* **9**, 70 (2018).
16. M. V. Hinckelmann *et al.*, Self-propelling vesicles define glycolysis as the minimal energy machinery for neuronal transport. *Nat Commun* **7**, 13233 (2016).
17. S. Jang *et al.*, Glycolytic Enzymes Localize to Synapses under Energy Stress to Support Synaptic Function. *Neuron* **90**, 278-291 (2016).
18. A. D. Wolfe *et al.*, Local and dynamic regulation of neuronal glycolysis in vivo. *Proc Natl Acad Sci U S A* **121**, e2314699121 (2024).
19. D. Zala *et al.*, Vesicular glycolysis provides on-board energy for fast axonal transport. *Cell* **152**, 479-491 (2013).
20. J. N. Spelbrink *et al.*, Human mitochondrial DNA deletions associated with mutations in the gene encoding Twinkle, a phage T7 gene 4-like protein localized in mitochondria. *Nat Genet* **28**, 223-231 (2001).
21. C. Kukat *et al.*, Super-resolution microscopy reveals that mammalian mitochondrial nucleoids have a uniform size and frequently contain a single copy of mtDNA. *Proc Natl Acad Sci U S A* **108**, 13534-13539 (2011).

22. C. M. Gustafsson, M. Falkenberg, N. G. Larsson, Maintenance and Expression of Mammalian Mitochondrial DNA. *Annu Rev Biochem* **85**, 133-160 (2016).
23. P. K. Hansma, B. Drake, O. Marti, S. A. Gould, C. B. Prater, The scanning ion-conductance microscope. *Science* **243**, 641-643 (1989).
24. P. Actis *et al.*, Compartmental genomics in living cells revealed by single-cell nanobiopsy. *ACS Nano* **8**, 546-553 (2014).
25. Y. Nashimoto *et al.*, Evaluation of mRNA Localization Using Double Barrel Scanning Ion Conductance Microscopy. *ACS Nano* **10**, 6915-6922 (2016).
26. N. L. Turner *et al.*, Reconstruction of neocortex: Organelles, compartments, cells, circuits, and activity. *Cell* **185**, 1082-1100 e1024 (2022).
27. S. C. Lewis, L. F. Uchiyama, J. Nunnari, ER-mitochondria contacts couple mtDNA synthesis with mitochondrial division in human cells. *Science* **353**, aaf5549 (2016).
28. N. Garrido *et al.*, Composition and dynamics of human mitochondrial nucleoids. *Mol Biol Cell* **14**, 1583-1596 (2003).
29. T. Kleele *et al.*, Distinct fission signatures predict mitochondrial degradation or biogenesis. *Nature* **593**, 435-439 (2021).
30. D. Poburko, J. Santo-Domingo, N. Demaurex, Dynamic regulation of the mitochondrial proton gradient during cytosolic calcium elevations. *J Biol Chem* **286**, 11672-11684 (2011).
31. P. J. Henderson, H. A. Lardy, Bongkrekic acid. An inhibitor of the adenine nucleotide translocase of mitochondria. *J Biol Chem* **245**, 1319-1326 (1970).
32. M. A. Lobas *et al.*, A genetically encoded single-wavelength sensor for imaging cytosolic and cell surface ATP. *Nat Commun* **10**, 711 (2019).
33. T. L. Lewis, Jr., G. F. Turi, S. K. Kwon, A. Losonczy, F. Polleux, Progressive Decrease of Mitochondrial Motility during Maturation of Cortical Axons In Vitro and In Vivo. *Curr Biol* **26**, 2602-2608 (2016).
34. A. Lee, Y. Hirabayashi, S. K. Kwon, T. L. Lewis, F. Polleux, Emerging roles of mitochondria in synaptic transmission and neurodegeneration. *Curr Opin Physiol* **3**, 82-93 (2018).
35. Y. Kirichok, G. Krapivinsky, D. E. Clapham, The mitochondrial calcium uniporter is a highly selective ion channel. *Nature* **427**, 360-364 (2004).
36. D. Chretien *et al.*, Mitochondria are physiologically maintained at close to 50 degrees C. *PLoS Biol* **16**, e2003992 (2018).
37. M. Terzioglu *et al.*, Mitochondrial temperature homeostasis resists external metabolic stresses. *Elife* **12**, (2023).
38. A. F. Oberhauser, J. R. Monck, J. M. Fernandez, Events leading to the opening and closing of the exocytotic fusion pore have markedly different temperature dependencies. Kinetic analysis of single fusion events in patch-clamped mouse mast cells. *Biophys J* **61**, 800-809 (1992).
39. Q. Chen *et al.*, Rewiring of Glutamine Metabolism Is a Bioenergetic Adaptation of Human Cells with Mitochondrial DNA Mutations. *Cell Metab* **27**, 1007-1025 e1005 (2018).
40. J. Nikkanen *et al.*, Mitochondrial DNA Replication Defects Disturb Cellular dNTP Pools and Remodel One-Carbon Metabolism. *Cell Metab* **23**, 635-648 (2016).
41. J. M. Cioni *et al.*, Late Endosomes Act as mRNA Translation Platforms and Sustain Mitochondria in Axons. *Cell* **176**, 56-72 e15 (2019).
42. M. Spillane, A. Ketschek, T. T. Merianda, J. L. Twiss, G. Gallo, Mitochondria coordinate sites of axon branching through localized intra-axonal protein synthesis. *Cell Rep* **5**, 1564-1575 (2013).
43. M. F. Gulen *et al.*, cGAS-STING drives ageing-related inflammation and neurodegeneration. *Nature* **620**, 374-380 (2023).

44. S. Victorelli *et al.*, Apoptotic stress causes mtDNA release during senescence and drives the SASP. *Nature* **622**, 627-636 (2023).
45. J. Goldsmith, A. Ordureau, J. W. Harper, E. L. F. Holzbaur, Brain-derived autophagosome profiling reveals the engulfment of nucleoid-enriched mitochondrial fragments by basal autophagy in neurons. *Neuron* **110**, 967-976 e968 (2022).
46. G. Ashrafi, J. S. Schlehe, M. J. LaVoie, T. L. Schwarz, Mitophagy of damaged mitochondria occurs locally in distal neuronal axons and requires PINK1 and Parkin. *J Cell Biol* **206**, 655-670 (2014).
47. M. Inan *et al.*, Energy deficit in parvalbumin neurons leads to circuit dysfunction, impaired sensory gating and social disability. *Neurobiol Dis* **93**, 35-46 (2016).
48. D. J. Surmeier, J. A. Obeso, G. M. Halliday, Selective neuronal vulnerability in Parkinson disease. *Nat Rev Neurosci* **18**, 101-113 (2017).
49. S. Pistor, T. Chakraborty, K. Niebuhr, E. Domann, J. Wehland, The ActA protein of Listeria monocytogenes acts as a nucleator inducing reorganization of the actin cytoskeleton. *EMBO J* **13**, 758-763 (1994).
50. W. Zhu *et al.*, Bcl-2 mutants with restricted subcellular location reveal spatially distinct pathways for apoptosis in different cell types. *EMBO J* **15**, 4130-4141 (1996).
51. J. Moffat *et al.*, A lentiviral RNAi library for human and mouse genes applied to an arrayed viral high-content screen. *Cell* **124**, 1283-1298 (2006).
52. L. A. Masullo *et al.*, Enhanced photon collection enables four dimensional fluorescence nanoscopy of living systems. *Nat Commun* **9**, 3281 (2018).
53. J. Alvelid, I. Testa, Stable stimulated emission depletion imaging of extended sample regions. *Journal of Physics D: Applied Physics* **53**, (2019).
54. J. Schindelin *et al.*, Fiji: an open-source platform for biological-image analysis. *Nat Methods* **9**, 676-682 (2012).
55. F. Wang *et al.*, RNAscope: a novel in situ RNA analysis platform for formalin-fixed, paraffin-embedded tissues. *J Mol Diagn* **14**, 22-29 (2012).
56. A. N. Player, L. P. Shen, D. Kenny, V. P. Antao, J. A. Kolberg, Single-copy gene detection using branched DNA (bDNA) in situ hybridization. *J Histochem Cytochem* **49**, 603-612 (2001).
57. C. Deleage *et al.*, Defining HIV and SIV Reservoirs in Lymphoid Tissues. *Pathog Immun* **1**, 68-106 (2016).
58. C. Wang, M. A. Telpoukhovskaia, B. A. Bahr, X. Chen, L. Gan, Endo-lysosomal dysfunction: a converging mechanism in neurodegenerative diseases. *Curr Opin Neurobiol* **48**, 52-58 (2017).

Acknowledgments: We thank members of the Lewis, Hirabayashi and Polleux labs for their comments on the manuscript. Qiaolian Zhang for excellent technical assistance. We thank Pierre Vanderhaeghen for suggestions on the manuscript.

Main figures and figure legends

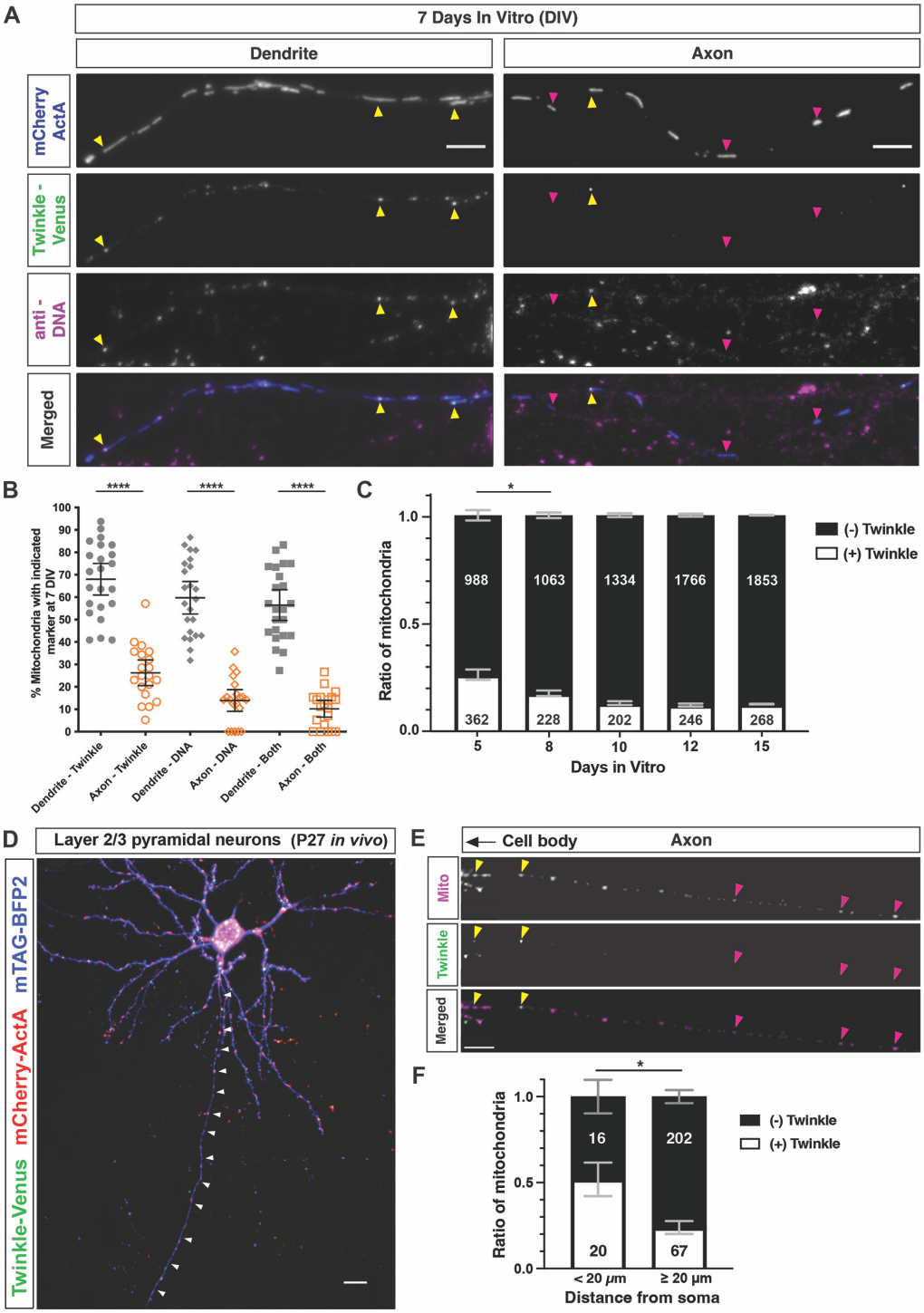

Figure 1
Hirabayashi, Lewis et al.

Figure 1. A low fraction of axonal mitochondria contain mtDNA and mtDNA-associated proteins compared to dendritic mitochondria of cortical pyramidal neurons *in vitro* and *in vivo*. (**A**) Representative dendritic (left) or axonal (right) segments from CPNs at 7DIV expressing mCherry-ActA (blue) to visualize mitochondria, Twinkle-Venus (green) to visualize the mitochondrial nucleoid and stained with an anti-DNA antibody (magenta) to directly visualize mtDNA. DNA+/Twinkle+ mitochondria are indicated by yellow arrows and DNA-/Twinkle- mitochondria are indicated by magenta arrows. (**B**) Quantification of the percentage of mitochondria with the indicated marker in dendrites or axons (each dot is an individual segment). $N_{dendrite}$ = 318 mitochondria from 23 dendrite segments, N_{axon} = 298 mitochondria from 20 axon segments from 3 independent experiments. **** $p \leq 0.0001$ by Kruskal-Wallis test. Error bars are 95% confidence intervals of the mean. (**C**) Quantification of the number of axonal mitochondria Twinkle+ at each DIV with mean ± SEM (5DIV neurons: n = 4 independent dishes and 8 or 10 or 12 or 15DIV neurons: n = 3 independent dishes). Numbers of mitochondria are indicated in each column. * $p < 0.05$ by unpaired t-test. (**D-E**) Representative images of a layer 2/3 CPNs *in vivo* (D; its axon highlighted by arrowheads) expressing mTag-BFP2 (blue), Twinkle-Venus (green) and OMM-targeted mCherry-ActA (red) at P27. The proximal portion of its axon is shown at higher magnification (E) with mCherry-ActA pseudocolored in magenta and Twinkle-Venus in green. Yellow arrowheads indicate Twinkle+ mitochondria in proximal part of axon, magenta arrowheads indicate Twinkle- mitochondria in more distal portion of axon. Scale bar: 10 µm. (**F**) Ratio of mitochondria either Twinkle positive (+) or negative (-) in the proximal (< 20 µm) or distal (> 20 µm) portion of the axon emerging from the soma are shown. Numbers of mitochondria counted are shown in each column. 13 neurons from 3 mice were used for quantifications. * $p = 0.013$ by paired t-test.

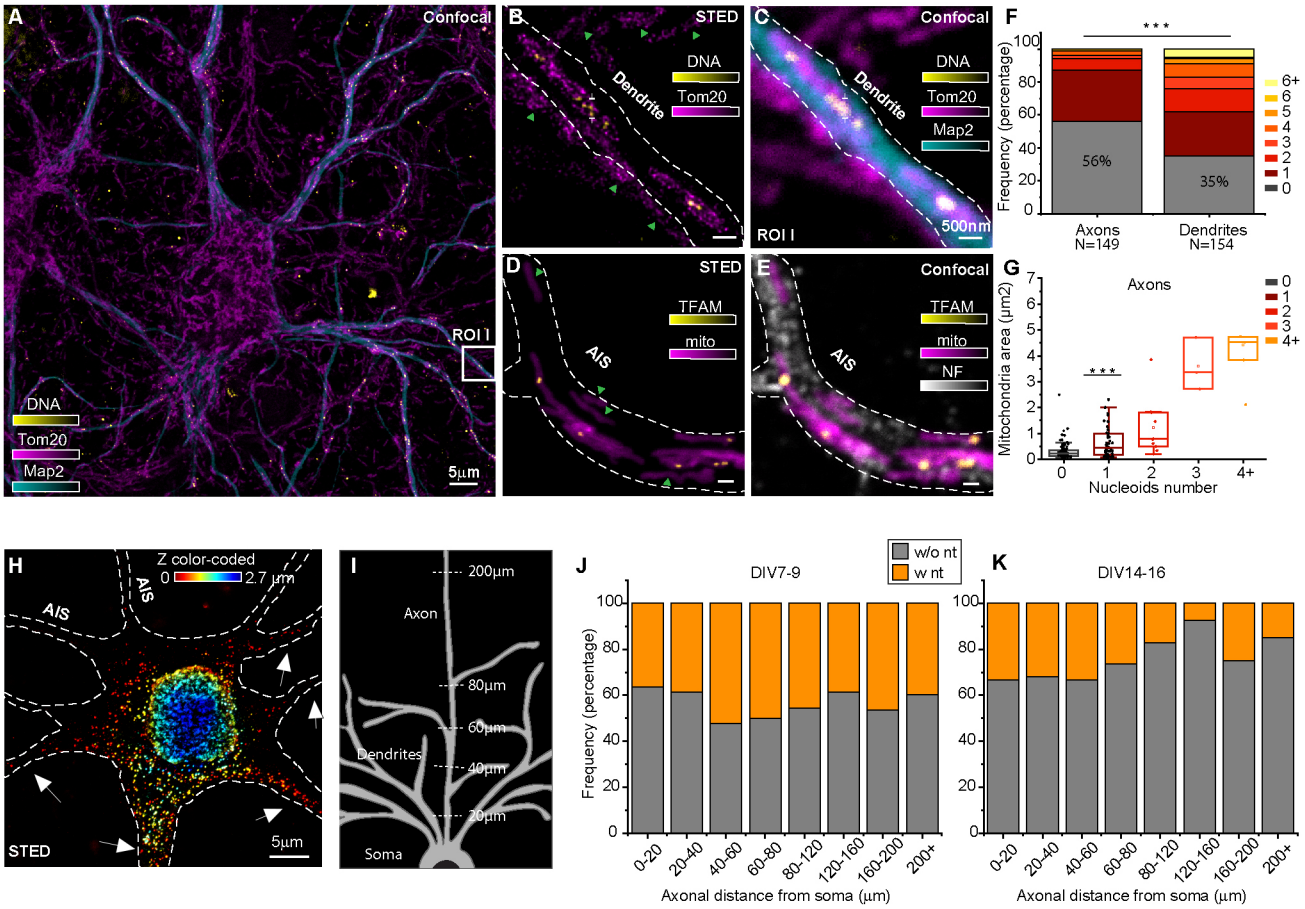

Figure 2
Hirabayashi, Lewis et al.

Figure 2. Super resolution imaging of mitochondria nucleoids in primary rat hippocampal neurons **(A)** Large confocal image overview of a neuron in culture showing the organization of mitochondrial DNA in nucleoids; nucleoids are immunostained for DNA, mitochondria for the outer membrane protein TOM20; dendrites (cyan) for the microtubule associated protein MAP2. **(B)** Two-color STED image of nucleoids from the Region of Interest (ROI) highlighted in A, where single nucleoids are visible in the STED image (white arrows), but are unresolved in the confocal comparison **(C)**; Nucleoids are not detectable in mitochondria outside the dendritic filament (green arrows), which probably belong to axons, wrapping around the dendrite. **(D-E)** Two-color STED image and relative confocal comparison of TFAM and mitochondria (mito) along the axon initial segment (AIS) labelled with the membrane protein neurofascin (NF). Mitochondria without nucleoids are common in the AIS (green arrows) **(F)** Frequency

of mitochondria without (grey) and with (1-6+) nucleoids detected in axons and dendrites ($N_{mitochondria}$= 303). * $p < 0.001$ by Kolmogorov-Smirnov test (KS-Test). **(G)** Box plot representation of the mitochondria area as a function of nucleoids number in each mitochondrion for axons. * $p < 0.001$ by Kolmogorov-Smirnov test (KS-Test). **(H)** 2D-STED volumetric image showing the spatial distribution of nucleoids across the cell soma. Nucleoids are barely visible along the axon, identified via the AIS staining (not shown) **(I)** Sketch of a neuron where the soma, dendrites and axons are represented to indicate the location of quantification shown in panels J-K. (**J-K**) Frequency of mitochondria without (grey) and with (yellow) nucleoids detected along the axon (zero at AIS emergence from soma) in immature (J; 7-9DIV) ($N_{mitochondria}$= 325) and mature (K; 14-16DIV) rat hippocampal neurons ($N_{mitochondria}$= 404).

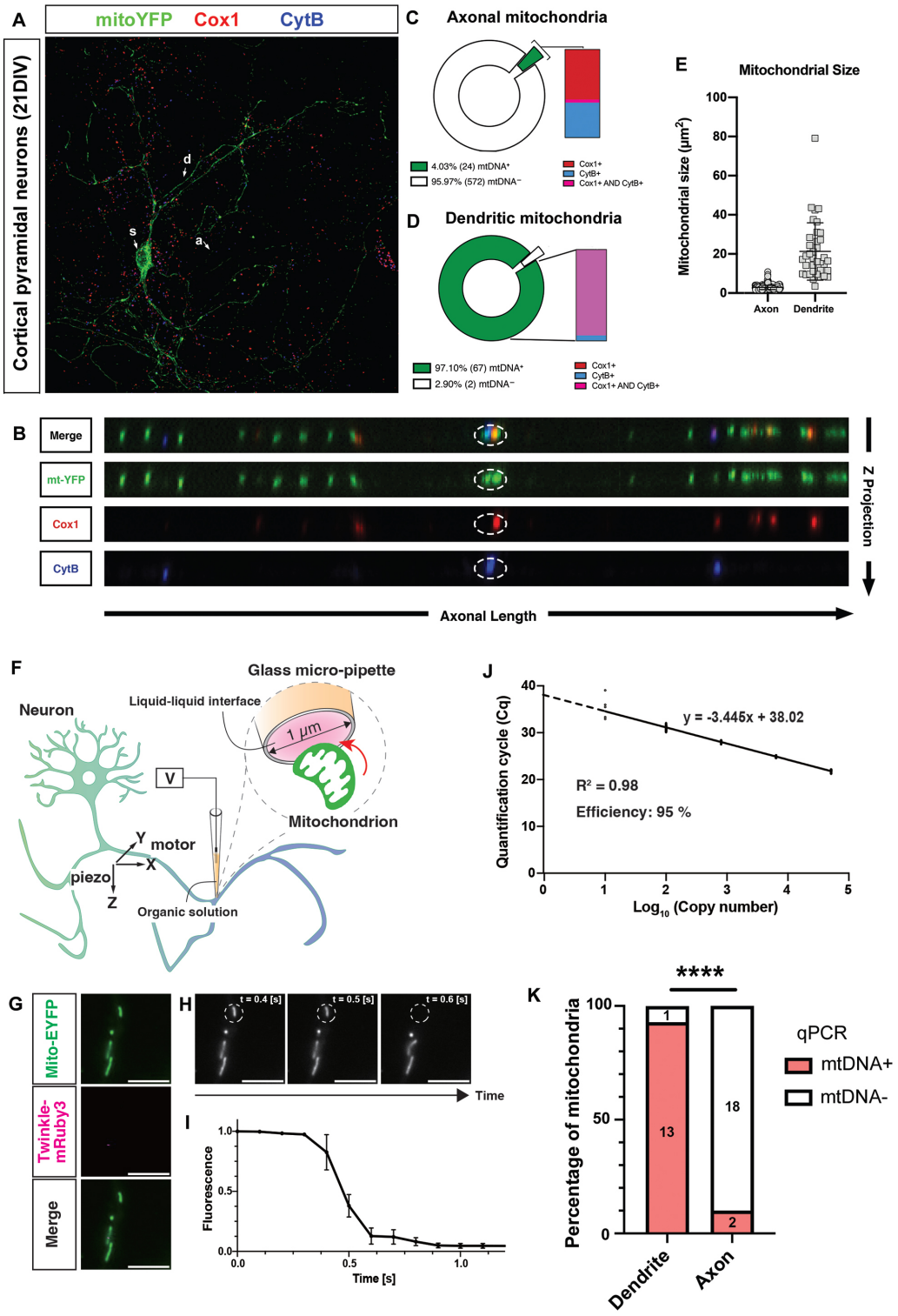

Figure 3

Hirabayashi, Lewis et al.

Fig. 3. DNA-FISH and single axonal mitochondria isolation coupled with quantitative PCR confirm the low fraction of mtDNA+ mitochondria in axons of CPNs.

(A-B) Low magnification (A) of a single cortical pyramidal neuron at 21DIV expressing matrix-targeted YFP (mito-YFP) following DNA-FISH detection of two mitochondria genes Cox1 (red) and Cytochrome B (blue). Abbreviations- s: soma; d: dendrites; a: axon. High magnification (B) confocal z-projection of multiple mitochondria along the axon highlighting a single mitochondrion co-localized with both Cox1 and CytB DNA-FISH signal (circled). (**C-D**) Quantification of Cox1+, CytB+ or double positive mitochondria along the axon (C) and dendrites (D) of CPNs in culture demonstrating that the majority of axonal mitochondria (>95%) of mitochondria are positive for either or both Cox1 or CytB DNA-FISH signals, whereas both mtDNA genes are detected in the majority of dendritic mitochondria in the same neurons. (**E**) Quantification of mitochondria size (surface area) in axons and dendrites in CPNs imaged for DNA-FISH experiments. Each point is an individual segment. N_{axon} = 596 mitochondria, 24 segments; $N_{dendrites}$ = 60 mitochondria, 6 segments.

(F) Schematic illustration of single axonal mitochondria extraction from mouse primary neocortical neurons using a nanopipette with an Ag/AgCl electrode. Upon changing the voltage across the organic solution/aqueous solution interface, an extraction force is applied to a mitochondrion in 7-9DIV neurons. **(G)** Virtually all neurons were infected with a lentivirus coding Mito-EYFP (green), while a fraction of neurons were electroporated with a plasmid coding Twinkle-mRuby3 (magenta). **(H)** A pipette was positioned close to a labeled axonal mitochondrion (dashed circle; t = 0.4 s). By changing the voltage, the mitochondrion was trapped into the tip (t = 0.5 s) and subsequently removed from the neuron (t = 0.6 s). Scale bar, 5 µm. **(I)** Changes of the EYFP fluorescence in areas corresponding to targeted mitochondria were plotted with mean±SEM (n = 7 independent measurements). **(J)** A calibration curve was created using serially diluted plasmids containing a mtDNA sequence corresponding to the sequence used to determine the copy number of mtDNA in each isolated axonal mitochondrion by qPCR. (**K**) Percentages of mitochondria in which mtDNA were detected. The numbers of mitochondria indicated in the bars were examined. **** $p < 0.001$ by Chi-square test.

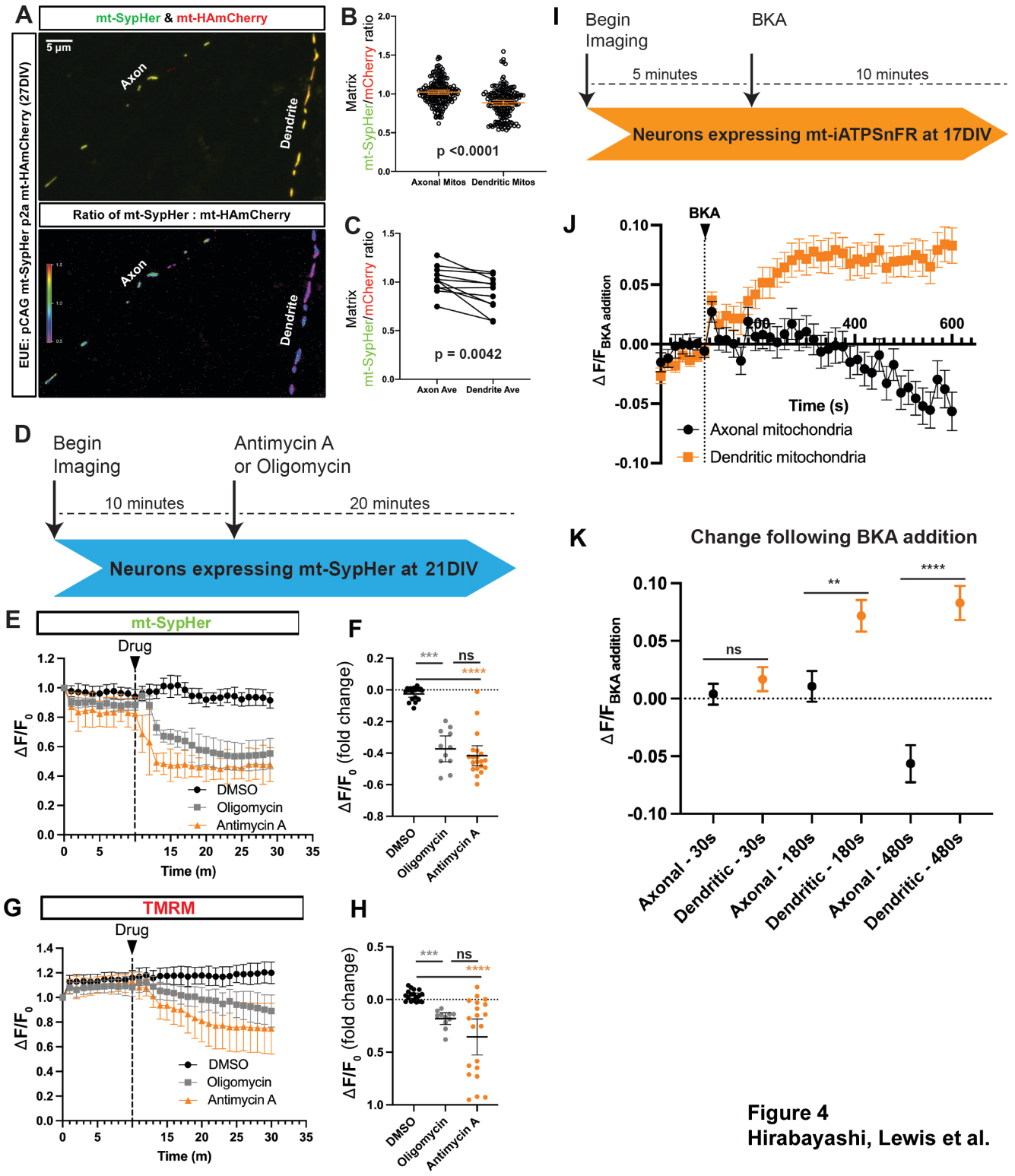

Fig. 4. Axonal mitochondria in CPNs run Complex V in reverse and consume ATP to maintain membrane potential.

(**A**) Axonal and dendritic mitochondria from the same neuron expressing mitochondrial matrix targeted SypHer (mt-SypHer) and HAmCherry (mt-HAmCherry) in culture for 21DIV. (**B-C**) Quantification of the SypHer to HA-mCherry ratio for individual, pooled mitochondria (B) or of paired axon and dendrite averages (C). A significant increased mt-SypHer/mCherry ratio in axonal compared to dendritic mitochondria suggests that the matrix of axonal mitochondria is more basic (lower H^+ concentration) than the matrix of dendritic mitochondria (**D**) Scheme for assaying axonal mitochondria responses following addition of either Antimycin A or Oligomycin. (**E-F**) Quantification of mt-SypHer fluorescence over time before and following addition of Antimycin A or Oligomycin (E) and average fold change of mt-SypHer fluorescence in individual axons (F). (**G-H**) Quantification of TMRM fluorescence over time before and following addition of either Antimycin A or Oligomycin (G) and average fold change of TMRM fluorescence in individual axons (H). Both Antimycin A and Oligomycin elicit acidification and loss of membrane potential in axonal mitochondria. (**I**) Scheme for assaying mitochondrial matrix ATP levels using matrix-targeted iATPSnFR1.0 (mt-iATPSnFR) in axonal and dendritic mitochondria of CPNs in culture at 17DIV. (**J**) Quantification of the change in matrix-targeted mt-iATPSnFR fluorescence in either dendritic mitochondria (orange) or axonal mitochondria (black) before and following BKA addition showing that dendritic matrix ATP increases with ANT blockade while axonal matrix ATP decreases with ANT blockade. (**J**) Fold change of mt-iATPSnFR 30 s, 180 s or 480 s after BKA addition in matrix of axonal and dendritic mitochondria. Scale bar in A is 5 µm. Error bars are SEM. **$p \leq 0.01$, *** $p \leq 0.001$, **** $p \leq 0.0001$. Kruskal-Wallis test for B, D, E and G. Paired t test for C. $N_{\text{mt-SypHer axonal}} = 167$ mitochondria from 11 neurons, 3 independent cultures, $N_{\text{mt-SypHer dendritic}} = 162$ mitochondria from 11 neurons, 3 independent cultures for B-C; $N_{DMSO} = 18$ axons from 3 independent cultures, $N_{\text{Antimycin A}} = 19$ axons from 3 independent cultures, $N_{\text{Oligomycin}} = 11$ axons from 3 independent cultures for E-H; $N_{\text{BKA axonal}} = 129$ mitochondria from 13 neurons, 3 independent cultures, $N_{\text{BKA dendritic}} = 110$ mitochondria from 13 neurons, 3 independent cultures for J-K.

Methods

Mice

All animals were handled according to protocols approved by the Institutional Animal Care and Use Committee (IACUC) at Columbia University, the Oklahoma Medical Research Foundation, University of Tokyo. Time-pregnant CD1 or ICR females were purchased from Charles Rivers. At the time of *in utero*,

or *ex utero* electroporation (E15.5), littermates were randomly assigned to experimental groups without regard to their sex.

Lentivirus production

HEK293T cells (RIKEN BRC, RCB2202) were co-transfected with shuttle vectors, VSV-G and Δ8.9 using FuGENE transfection reagent (Promega, E2311). 24 hours after transfection, the media was exchanged with fresh Neurobasal media (Gibco, 21103049), and 48 hours later, supernatants were harvested, spun at 2500×g to remove debris and filtered through a 0.45 μm filter (Membrane Solutions, PES025045). The filtered supernatant was concentrated ×20 using an Amicon® Ultra-15 centrifugal filter device (molecular weight cut-off 100 kDa, UFC910024, Merck Millipore Ltd.), which was centrifuged at 4,000×g for 20 minutes at 4°C. The concentrated samples were diluted with 1×PBS (Nissui, 05913) and stored at −80°C.

Plasmids

FUW mito-EYFP was created from FUIGW (kind gift from Dr. Yukiko Gotoh) by replacing the IG sequence with mito-EYFP sequence using EcoR1 and BsrG1 sites. pCAG HAmCherry-ActA was created by PCR of the DNA encoding HAmCherry and subcloning it 3' to the CAG promoter but 5' to the ActA mitochondrial targeting sequence (*49, 50*). pCAG Twinkle-venus was created by PCR of the DNA encoding mouse Twinkle from a neuronal mouse cDNA library, and subcloned 3' to the CAG promoter but 5' to the DNA encoding Venus YFP via Infusion cloning. pCAG Twinkle-mRuby3 was created from pCAG Twinkle-Venus by replacing the Venus YFP sequence with mRuby3 via infusion cloning, using Age1 and Not1 sites. pCAG mt-SypHer was created by PCRing the DNA encoding mt-SypHer from Addgene plasmid #48251 (a gift from Nicolas Demaurex), and subcloning it 3' to the CAG promoter. pCAG mt-SypHer p2a mt-HAmCherry was created by subcloning the DNA encoding 2xmt-HAmCherry 3' to pCAG mt-SypHer via Infusion cloning. pCAG 4xmt-iATPSnFR1.0 was created by PCR of the DNA encoding iATPSnFR1.0 from Addgene Plasmid #102556 (a gift from Baljit Khakh), and subcloning it 3' to the 4x synthetic mitochondrial targeting sequence in Addgene plasmid #66896 (a gift from Georg Ramm). This whole DNA encoding the 4x-mt iATPSnFR1.0 was then subcloned 3' to the CAG promoter via infusion cloning.

***In utero* electroporation**

A mix of endotoxin-free plasmid preparation (2 mg/mL total concentration) and 0.5% Fast Green (Sigma) was injected into one lateral hemisphere of E15.5 embryos using a Picospritzer III (Parker). Electroporation (ECM 830, BTX, CUY21EDITII) was performed with gold paddles to target cortical progenitors in E15.5 embryos by placing the anode (positively charged electrode) on the side of DNA injection and the cathode on the other side of the head. Five pulses of 45 V for 50 ms with 500 ms interval were used for electroporation. Animals were sacrificed 21 days after birth (P21) by terminal perfusion of 4% paraformaldehyde (PFA, Electron Microscopy Sciences) followed by overnight post-fixation in 4% PFA.

Ex utero cortical electroporation

A mix of endotoxin-free plasmid preparation (2-5 mg/mL) and 0.5% Fast Green (Sigma) mixture was injected using a Picospritzer III (Parker) into the lateral ventricles of isolated head of E15.5 mouse embryo, and electroporated using an electroporator (ECM 830, BTX) with four pulses of 20 V or five pulses of 22 V (for the single mitochondria isolation experiments) for 100 ms with a 500 ms interval. Following *ex utero* electroporation, we performed dissociated neuronal culture as described below.

Primary neuronal culture

Embryonic mouse cortices (E15.5) were dissected in Hank's Balanced Salt Solution (HBSS) supplemented with HEPES (10 mM, pH7.4), and incubated in HBSS containing papain (Worthington; 14 U/ml) and DNase I (100 μg/ml) for 20 min at 37°C. Then, samples were washed with HBSS, and dissociated by pipetting. Cell suspension was plated on poly-D-lysine (1 or 0.2 mg/ml, Sigma)-coated glass bottom dishes (MatTek) or coverslips (BD bioscience) in Neurobasal media (Invitrogen) containing B27 (1x), Glutamax (1x), FBS (2.5%) and penicillin/streptomycin (0.5x, all supplements from Invitrogen). Every 5 to 7 days, one third of the media was exchanged with supplemented Neurobasal media without FBS.

Primary neuronal culture at a physiological glucose concentration

Mouse neurons were cultured for the first 4 DIV in Neurobasal media containing B27 (1x), Glutamax (1x), FBS (2.5%). At 4DIV, the half of the media was exchanged with a supplemented BrainPhys Imaging Optimized media (STEMCELL Technologies) without FBS. Half-medium changes were performed every 3 to 4 days.

Immunocytochemistry

Primary culture - Cells were fixed for 10 minutes at room temperature in 4% (w/v) paraformaldehyde (PFA, EMS) in PBS (Sigma), then incubated for 30 minutes in 0.1% Triton X-100 (Sigma), 1% BSA (Sigma), 5% Normal Goat Serum (Invitrogen) in PBS to permeabilize and block nonspecific staining, after washing with PBS. Primary and secondary antibodies were diluted in the buffer described above. Primary antibodies were incubated at room temperature for 1-2 hours and secondary antibodies were incubated for 30 minutes at room temperature. Coverslips were mounted on slides with Fluoromount G (EMS). Primary antibodies used for immunocytochemistry in this study are chicken anti-GFP (5 µg/ml, Aves Lab – recognizes GFP and YFP), mouse anti-HA (1:500, Covance), rabbit anti-RFP (1:1,000, Abcam – recognizes mTagBFP2, DsRED and tdTomato), mouse anti-DNA (1:200, American Research Products Inc). All secondary antibodies were Alexa-conjugated (Invitrogen) and used at a 1:2000 dilution. Nuclear DNA was stained using Hoechst 33258 (1:10,000, Pierce)

Brain sections - Post fixed brains were sectioned via vibratome (Leica VT1200) at 100 µm. Floating sections were then incubated for 2 hours in 0.4% Triton X-100, 1% BSA, 5% Normal Goat Serum in PBS to block nonspecific staining. Primary and secondary antibodies were diluted in the buffer described above. Primary and secondary antibodies were incubated at 4°C overnight. Sections were mounted on slides and coversliped with Aqua PolyMount (Polymount Sicences, Inc). Primary and secondary antibodies are the same as above.

Imaging

Fixed samples were imaged on a Nikon Ti-E microscope with an A1 confocal. All equipment and solid state lasers (Coherent, 405 nm, 488 nm, 561 nm, and 647 nm) were controlled via Nikon Elements software. Nikon objectives used include 20x (0.75NA), 40x (0.95NA) or 60x oil (1.4NA). Optical sectioning was performed at Nyquist for the longest wavelength. Analysis of mitochondrial length and occupancy were performed in Nikon Elements.

Live imaging - Electroporated cortical neurons were imaged at 7-21DIV with EMCCD (Andor, iXon3-897) or sCMOS (Hamamatsu Orca Fusion) on an inverted Nikon Ti-E microscope or Nikon Ti2-E (40x objective NA0.95 with 1.5x digital zoom or 60x objective NA1.4) with Nikon Elements. 488 nm and 561nm lasers shuttered by Acousto-Optic Tunable Filters (AOTF) or 395 nm, 470 nm, and 555 nm Spectra X LED lights (Lumencor) were used for the light source, and a custom quad-band excitation/dichroic/emission cube (based off Chroma, 89400) followed by clean up filters (Chroma,

ET435/26, ET525/50, ET600/50) were applied for excitation and emission. We used cHBSS as the imaging solution.

For Tetramethylrhodamine (Sigma, TMRM) imaging cells were incubated with 10 nM TMRM for 20 minutes at 37°C to load the cells before imaging started. TMRM was maintained in the imaging buffer at 5 nM throughout the experiment.

For experiments using mitochondrial toxins, cells were imaged for a base line period then the indicated drug was bath applied at the indicated time points. Antimycin A and Oligomycin were used at 1.25 μM final concentration. Bongkrekic Acid was used at 50 μM final concentration.

Images were analyzed using the time series module in NIS Elements. Full-length mitochondria were marked by a freehand selection tool intensities were measured. After intensities were corrected for background subtraction, ΔF values were calculated from ($F-F_0$).

Single mitochondria extraction

Single mitochondria extraction was performed using an epifluorescence microscope equipped with a nanopipette. Our homemade nanopipette system consisted of a 40 × 40 μm travel range XY piezo stage (PK2H100-040U, THK precision) and a homemade 9.1 μm travel range Z piezo stage equipped with a piezoelectric actuator (AE0505D08, NEC Tokin) for controlling the nanopipette along the Z-axis. A stepping motor stage with a travel range of 30 mm (KXG06030-G, SURUGA SEIKI) was used for coarse positioning of the nanopipette along the Z-axis. The XY and Z piezo stages were operated by a capacitive sensor-controlled closed-loop piezo controller (NCM7302C, THK precision) and an open loop piezo driver (PH103, THK precision), respectively. The pipette current was detected via a homemade 1 GΩ feedback resistance current amplifier. The stable power supply (LP5392, NF) was used as a homemade current amplifier. The holding voltage for the ion current measurement was supplied by a Digital Analog converter of a field-programmable gate array (USB-7855R OEM, National Instruments) to the Ag/AgCl electrode placed in a solution around the cell.

The glass nanopipettes (inner radius, 1.0 μm) were fabricated from a borosilicate glass capillary (GC100F-15, Harvard Apparatus) using a CO_2 laser puller (model P-2000, Sutter Instruments) and were filled with a solution of 1–2 dichlorethane containing 10 mM tetrahexylammonium tetrakis(4-chlorophenyl)borate (THATPBCl). Ag/AgCl electrodes were inserted into the micropipette.

To visualize all the mitochondria in a dish, cells electroporated with Twinkle-mRuby3 were infected with lentivirus carrying Mito-EYFP. Voltage was applied to the liquid-liquid interface between dichlorethane

in the nanopipette and the culture media in the dish to control the dichlorethane surface tension. To prevent the solution from flowing into the nanopipette before extraction, the voltage was kept at +0.5 V vs Ag/AgCl. After positioning the nanopipette tip close to a target mitochondrion, the voltage was changed to -1.0 V for 300-500 ms to rise the oil-water interface and extract the mitochondrion into the nanopipette. After confirming the disappearance of the target mitochondrial signal from the cell, the mitochondrion was collected in a 96-well plate (Greiner, 669285) by breaking off the tip of nanopipette. Cells were imaged with an IX83 Olympus microscope equipped with an X-Cite XYLIS illuminator (Excelitas Technologies, XT720S), ORCA-Fusion CMOS camera (Hamamatsu Photonics, C14440-20UP), and ×100 objective (Olympus, UPLXAPO100XO, NA 1.45).

Quantitative PCR (qPCR) Assay for mtDNA detection

The template plasmid was constructed as follows; a part of mitochondrial DNA encoding 12S rRNA (chrM: 484-1,018) was amplified from DNA extracted from NIH-3T3 cells (RIKEN BRC, RCB2767) and cloned into pBluescript II SK(-), followed by confirmation by DNA sequencing. The copy number of plasmids per microliter was calculated from the concentration measured by NanoDrop One (Thermo Scientific™) and molecular weight of the plasmid. The template plasmid was diluted to 5×10^7 copies/μL with nuclease-free water plus yeast RNA (Roche, 10109223001), and this solution was further diluted to 2.5, 25, 200, 1600, and 12800 copies/μL and used for generating a standard curve. Low-binding tips (BMBio, W200-RS, FastGene, FGF-20LA) and low-binding tubes (Eppendorf, 0030108434) were used for dilution.

All qPCR reactions were run on a LightCycler 96 (Roche, 05815916001) using a QuantiNova Probe PCR Kit (Qiagen, 208254) following the kit protocol. qPCR amplification experiments were carried out in a 20 μL reaction volume consisting of 2× QuantiNova Probe PCR Master Mix, 0.4 μM dual-color probe, 0.2 μM forward and reverse primers, and nuclease-free water. The qPCR primer pairs (Fw: 5'-CTACCTCACCATCTCTTGCTAAT-3', Rv: 5'-TTGGCTACACCTTGACCTAAC-3') and the probe (5'-HEX-ATACCGCCA-ZEN-TCTTCAGCAAACCCT-IABkFQ-3') were purchased from Integrated DNA Technologies. After an initial denaturation cycle of 95°C for 2 min, 50 PCR cycles were performed (denaturation at 95°C for 5 s, and annealing/extension at 60°C for 5 s). The quantification cycle (Cq) values (the number of PCR cycles at which the fluorescence amplification curve of a sample intersects the threshold line) were calculated using the fit points method of the LightCycler 96 software. The Cq values

of the samples were fitted to the standard curve to determine the copy number of mtDNA, and those with the copy number < 1 were defined as mtDNA negative.

Quantification and Statistical Analysis

All statistical analysis and graphs were performed/created in Graphpad's Prism 9. Statistical tests, p values, and (n) numbers are presented in the figure legends. Gaussian distribution was tested using D'Agostino & Pearson's omnibus normality test. We applied non-parametric tests when data from groups tested deviated significantly from normality. All analysis were performed on raw imaging data without any adjustments. Images in figures have been adjusted for brightness and contrast (identical for control and experimental conditions in groups compared).

Resources

REAGENT or RESOURCE	SOURCE	IDENTIFIER
Antibodies		
Chicken anti-GFP	Aves	GFP-1020
Mouse anti-HA.11 – Clone 16B12	Covance	MMS-101R
Rabbit anti-RFP	Abcam	Ab62341
Mouse anti-DNA	American Research Products Inc	03-61014
Rabbit anti-ERp72 (D70D12)	Cell Signaling Tech	5033S
Rabbit anti-Tom20	Abcam	ab78547
Mouse anti-DNA	Progen Biotechnik	61014
Rabbit anti-TFAM	Abcam	ab131607
Chicken anti-Map2	Abcam	ab5392
Rat anti-Pan-Neurofascin	UC Davis/NIH NeuroMab Facility	75-172
Rabbit anti-GFP	Abcam	ab6556
Goat-anti-rabbit-AF594	Thermo Fisher Sci	A-11037
donkey-anti-mouse-AF594	Thermo Fisher Sci	A-21203
goat-anti-rabbit-S635P	Abberior	2-0012-007-2
goat-anti-mouse-S635P	Abberior	2-0002-007-5
goat-anti-mouse-AF488	Thermo Fisher Sci	A-11001

goat-anti-chicken-AF488	abcam	ab150173
goat-anti-mouse-DyLight405	Thermo Fisher Sci	35501BID
FluoTag®-X4 anti-GFP	NanoTag Biotech.	N0304-Ab580
FluoTag®-X4 anti-GFP	NanoTag Biotech.	0304-Ab635-L
Kits		
Infusion HD Cloning Plus	Clontech	638911
QuantiNova Probe PCR Kit	Qiagen	208254
Lipofectamine 2000 Transfection Reagent	Thermo Fisher Sci	11668019
Chemicals, Peptides, and Recombinant Proteins		
Fast Green	Sigma	F7258
Hank's Balance Salt Solution	Thermo Fisher Sci	14185-052
HEPES	Thermo Fisher Sci	15630-080
B27 Supplement	Thermo Fisher Sci	17504-004
GlutaMAX	Thermo Fisher Sci	35050-061
Neurobasal	Thermo Fisher Sci	21103-049
Penicillin/Streptomycin	Thermo Fisher Sci	15140-122
Papain	Worthington	LK003178
DNase	Sigma	D5025
Poly-D-Lysine	Sigma	P0899
Fetal Bovine Serum	Gemini Bio-Products	100-500
Normal Goat Serum	Thermo Fisher Sci	16210-064
BSA	Sigma	A7906
PBS	Sigma	P4417
NaCl	Sigma	746398
KCl	Sigma	P5405
NaH_2PO_4	Sigma	S5011
$CaCl_2$	Sigma	C5670
Glucose	Sigma	G7021
NH_4Cl	Sigma	A9434
Tetramethylrhodamine methyl ester perchlorate (TMRM)	Sigma	T5428
Trizma	Sigma	T1503

Trizma-HCl	Sigma	T3253
$MgCl_2$	Sigma	M4880
Protease and phosphatase cocktail inhibitors	Sigma	11836170001
Benzonase	EMD Millipore	70664-3
EDTA	Sigma	E6758
NP-40	Sigma	NP40
Triton X-100	Sigma	X100
Tween 20	Sigma	P9416
FCCP	Sigma	C2920
Antimycin A	Sigma	A8674
Oligomycin	Sigma	O4876
Bongkrekic Acid	Sigma	B6179
FuGENE transfection reagent	Promega	E2311
Neurobasal medium	Gibco	21103049
PBS	Nissui	05913
MitoBright LT Green	Dojindo	MT10
NaCl	FUJIFILM Wako	190-13921
KCl	FUJIFILM Wako	163-03545
$CaCl_2$	Nacalai tesque	08894-25
$MgCl_2$	FUJIFILM Wako	133-15051
HEPES	Thermo Fisher Sci	15630106
Glucose	FUJIFILM Wako	047-31161
Yeast RNA	Roche	10109223001
Minimum Essential Medium, MEM	Thermo Fisher Sci	21090022
poly-D-ornithine	Sigma Aldrich	P8638
HEPES	Thermo Fisher Sci	15630-080
B27 Supplement	Thermo Fisher Sci	17504-004
Horse Serum	Thermo Fisher Sci	26050088
Neurobasal	Thermo Fisher Sci	21103-049
Penicillin/Streptomycin	Sigma Aldrich	P4333
L-Glutamine	Thermo Fisher Sci	25030-024
Sodium pyruvate	Thermo Fisher Sci	11360-070

NaCl	Sigma	746398
KCl	Sigma	P5405
CaCl2 · 2H2O	Sigma	C3881
MgCl2 * 6 H2O	Sigma	M2670
Triton X-100	Sigma	X100
Glucose	Sigma	D8375
BSA	Sigma	A7906
Paraformaldehyde	Sigma	P6148
DABCO	Thomas Scientific	C966M75
Experimental Models: Cell Lines		
Human: HEK cells	ATCC	CRL-11268
Human: HEK293T cells	RIKEN BRC	RCB2202
Mouse: NIH3T3 cells	RIKEN BRC	RCB2767
Experimental Models: Organisms/Strains		
Mouse: CD1 IGS	Charles River Labs	Strain Code: 022
Mouse: Slc:ICR	SLC	
Rat: Sprague Dawley	Janvier Labs	Strain: RjHan:SD
Oligonucleotides		
Mff shRNA: CCGGGATCGTGGTTACAGGAAATAACTCGAGTTATTTCCTGTAACCACGATCTTTTTTG	Sigma	TRCN0000174665
Control shRNA: CCGCAGGTATGCACGCGT	(*51*)	Addgene Plasmid 10879
Recombinant DNA		
pCAG HAmCherry-ActA	This paper	N/A
pCAG Twinkle-venus	This paper	N/A

pCAG TFAM-tdTomato	This paper	N/A
pCAG mt-YFP	(*33*)	N/A
pCAG mt-SypHer	This paper	N/A
pCAG mt-SypHer p2a mt-HAmCherry	This paper	N/A
pCAG 4xmt-iATPSnFR1.0	This paper	N/A
pCAG 4xmt-mScarlet-iATPSnFR1.0	This paper	N/A
pCAG mTAGBFP2	(*10*)	N/A
pCAG mScarlet	(*10*)	Addgene Plasmid 85042
pLKO1.5	(*51*)	Addgene Plasmid 10879
FUW mito-YFP	This paper	N/A
FUW Twinkle-mRuby3	This paper	N/A
FUW Twinkle-mScarlet	This paper	N/A
pOMP25-rsEGFP2	(*52*)	N/A
Others		
#1.5 18 mm glass coverslips	Marienfeld	0117580
Software		
Imspector	Max-Planck-Innov.	
OriginPro2020	OriginLab	

Primary rat hippocampal neuron cultures

For Figure 2, experiments were performed in Ilaria Testa laboratory in accordance with animal welfare guidelines set forth by Karolinska Institutet and were approved by Stockholm Swedish Board of agriculture for Animal Research. Rats were housed with food and water available ad libitum in a 12 hours' light/dark environment.

Primary hippocampal cultures were prepared from embryonic day 18 (E18) Sprague Dawley rat embryos. The pregnant mothers were sacrificed with CO2 inhalation and aorta cut; brains were extracted from the embryos. Hippocampi were dissected and mechanically dissociated in Minimum Essential Medium, MEM, (Thermo Fisher Scientific). 40 x 10^3 cells per well were seeded in 12 well plates on a poly-D-ornithine (Sigma Aldrich) coated #1.5 18 mm glass coverslips (Marienfeld,) and let them attach in MEM

with 10% Horse Serum (Thermo Fisher Scientific), 2 mM L-Glut (Thermo Fisher Scientific) and 1mM Sodium pyruvate (Thermo Fisher Scientific), at 37°C at an approximate humidity of 95 – 98% with 5% CO2. After 3 hours the media was changed to Neurobasal Medium (Thermo Fisher Scientific) supplemented with 2% B-27 (Thermo Fisher Scientific), 2 mM l-Glutamine and 1% Penicillin-Streptomycin (Sigma Aldrich). The cultures were kept at 37°C at an approximate humidity of 95 – 98% with 5% CO2 for up to 24 days. Medium was changed twice per week. The experiments were performed on cultures starting from DIV7 up to DIV16.

Immunostaining of neuronal culture for STED imaging.

For data presented in Figure 2, rat neuronal cultures were washed in Artificial Cerebrospinal Fluid (ACSF) solution and then fixed in pre-warmed 4% paraformaldehyde (PFA) in phosphate buffered saline (PBS; pH 7.4) at RT for 15 minutes and permeabilized for 5 minutes in 0.1% Triton-X-100 buffer and blocked with 5% bovine serum albumin (BSA) (Sigma-Aldrich) in PBS, for 30 minutes at RT. Incubation with primary and secondary antibodies was performed in PBS solution for 1 hour at RT. Samples were mounted in custom-made Mowiol mounting media, supplemented with DABCO (Thomas Scientific).

Primary antibodies are listed and used as follows: anti-Tom20 (abcam, 1:200); anti-DNA (PROGEN Biotechnik, 1:100) ; anti-TFAM (abcam, 1:200); anti-Map2 (abcam, 1:2000); anti-Pan-Neurofascin (UC Davis/NIH NeuroMab Facility, 1:100), anti-GFP (abcam, 1:200). Secondary antibodies are listed and used as follows: Goat-anti-rabbit-AF594 (Thermo Fisher Scientific, 1:200 dilution), donkey-anti-mouse-AF594 (Thermo Fisher Scientific, 1:200 dilution); goat-anti-rabbit-S635P (Abberior, 1:200 dilution), goat-anti-mouse-S635P (Abberior,1:200 dilution); goat-anti-mouse-AF488 (Thermo Fisher Scientific, 1:200 dilution); goat-anti-chicken-AF488 (abcam, 1:200); goat-anti-mouse-DyLight405 (Thermo Fisher Scientific; 1:100), FluoTag®-X4 anti-GFP, (NanoTag, N0304-Ab580 or N0304-Ab635P-L).

Neuron transfection and live cell staining for STED imaging.

To stain the mitochondria outer membrane, neurons were transfected with OMP25-rsEGFP2 plasmid (*52*) using Lipofectamine 2000 Transfection Reagent (Thermo Fisher Scientific), according to the instructions of the manufacturer. To stain the AIS neuronal cultures were incubated for 5 minutes at RT with anti-pan-neurofascin primary antibody (UC Davis/NIH NeuroMab Facility, 1:100), subsequently washed three imes with ACSF buffer, then incubated with goat-anti-mouse-DyLight405 secondary antibody (Thermo Fisher Scientific; 1:100) for 5 minutes at 37°C and finally washed three times in ACSF buffer.

STED imaging

STED images were recorder with a custom-built STED setup, previously described (*53*). Excitation of the dyes was done with pulsed diode lasers; at 561 nm (PDL561, Abberior Instruments), 640 nm (LDH-D-C-640, PicoQuant) and 510 nm (LDF-D-C-510, PicoQuant). A laser at 775 nm (KATANA 08 HP, OneFive) was used as the depletion beam, which was split into two orthogonally polarized beams that were separately shaped to a donut and a top-hat respectively in the focal plane using a spatial light modulator (LCOS-SLM X10468-02, Hamamatsu Photonics). The laser beams were focused onto the sample using a HC PL APO 100×/1.40 Oil STED White objective (15506378, Leica Microsystems), through which the fluorescence signal was also collected. The images were recorder with a 561nm excitation laser power of 8–20 µW, a 640 nm excitation laser power of 4–10 µW and a 775 nm depletion laser power of 128 mW, measured at the first conjugate back focal plane of the objective. Two-color STED imaging was done in a line-by-line scanning modality. The pixel size was set between 20 and 30 nm with a pixel dwell time of 50 µs. Volumetric 2D-STED imaging of nucleoids was recorded with a voxel size for xyz volumes was set to 25 × 25 × 200 nm^3. The pixel dwell time was set at either 30 or 50 µs.

Image analysis of super-resolution (STED) microscopy

The images were processed and visualized using the ImSpector software (Max-Planck Innovation) and ImageJ(*54*). When necessary, images and movies were deconvolved using the Richardson-Lucy algorithm, implemented in Imspector. The PSF was modelled as a Gaussian function and the FWHM was chosen to be 40 nm. The regularization parameter and number of iterations were varied depending on the quality of the output image. The regularization parameter was set as either 10^{-5} while the number of iterations was chosen up to a maximum of 5. Brightness and contrast were linearly adjusted for the entire images. The data were then analysed, fitted and visualized with the software OriginPro2020 (OriginLab). To calculate the frequency of mitochondria without and with (1-6+) nucleoids in axons and dendrites, a analysis pipeline was developed: (i) the binary maps of soma, dendrites and axons were generate in ImageJ, based on the Map2 and Neurofascin staining; (ii) the mitochondria binary map was generated based on mitochondria staining; (iii) To measure the distribution of nucleoids per mitochondria along the axonal length, a semi-automatic pipeline was set-up. It consists of the following steps: (1) Binarize image of mitochondria and get center points of each mitochondria; (2) Detect maxima in TFAM image (glass-to-glass adjusted thresholding) and get the positions; (3) Count the number of maxima per binarized

mitochondria area; (4) Manually segment axon from AIS image and binarize; (5) Make a geodesic distance transform from manually selected seed point closest to the soma; (6) Check distance from each mitochondria center to the soma in the geodesic distance map. For comparison of distributions of parameters, the Kolmogorov-Smirnov test was chosen (KS-test). This choice was made due to the non-normal nature of the observed distributions.

DNAScope Fluorescent In Situ Hybridization (DNA-FISH) detection of mitochondrial DNA

For Figure 3A-E, Primary mouse layer 2/3 pyramidal neurons were ex utero electroporated at E15.5, immediately dissociated and plated at 100,000 cell density on 35 mm MatTek Dishes, cultured for either 14 or 21 days, and fixed in 4% paraformaldehyde for 15 minutes, followed by three, 5 minute washes with PBS (1X). The cells were then treated with RNAscope® Hydrogen Peroxide Reagent for ten minutes at 23°C to 25°C and washed twice with deionized water, followed by digestion in a 1:15 dilution of RNAscope® Protease III Reagent in PBS (1X) at 23°C to 25°C and two washes in PBS (1X). Immediately following hydrogen peroxide and protease treatment, the cells were incubated with an RNAse cocktail (RNase A at 20 U/mL; RNase T1 at 800 U/mL; Fisher Scientific) in PBS (1X) for 30 minutes at 37°C inside a HybEZ hybridization oven (ACD). The samples were then washed twice with PBS (1X) and then incubated with pre-warmed target probes (20 nmol/L of each oligo probe) overnight at 40ºC inside the HybEZ hybridization oven (ACD). CY-B was targeted with RNAscope® Probe- Mm-mt-Cytb (ACD;Cat No. 517301), and CO1 was targeted with RNAscope® Probe- Mm-mt-Co1-C2 (ACD;Cat No. 517121-C2). Following overnight target probe hybridization, the samples were incubated at 40°C in Amplifier 1 (preamplifier) (2 nmol/L) for 30 minutes; Amplifier 2 for 30 minutes; and Amplifier 3 (label probe) for 15 minutes at. After each hybridization step, slides were washed with wash buffer (0.1× SSC, 0.03% lithium dodecyl sulfate) two times at room temperature. Chromogenic detection was performed using a horseradish peroxidase (HPR) construct specific to each gene-dedicated imaging channel and a fluorescent Opal reagent of choice. CY-B was stained with Opal 520 Reagent (Perkin Elmer, FP1487001KT), and CO1 was stained with Opal 570 Reagent (Perkin Elmer, FP1488001KT). Each Opal reagent dye was diluted 1:1500 in RNAscope® Multiplex TSA Buffer. Coverslips were mounted onto slides in Fluoro-Gel (EMS; 17985-10**)** and imaged at 60x magnification.

Detection of mitochondrial genes, CY-B (cytochrome b) and CO1 (cytochrome c oxidase subunit 1) was conducted by *in situ* hybridization of specific targeting probes with a modified RNAscope Multiplex Fluorescent v2 Assay Protocol. The RNAscope targeting scheme has been previously described and

utilizes a pair of gene-specific double Z probes (ZZ) that together bind a contiguous region of approximately 50 bases on the target sequence. Each Z probe includes a spacer region and a 14-base tail sequence that, when aligned next to the other probe's tail sequence, generates a 28-base binding site for the preamplifier oligonucleotide (*55*). The preamplifier contains 20 binding sites for the amplifier, which, in turn, contains 20 binding sites for the label probe, allowing signal amplification similarly to the previously described branched DNA scheme (*56*). The double Z probe strategy confers high target specificity because amplification is dependent on both Z probes localizing to their target sequences to generate the 28-base landing site.

The modified protocol used for labeling DNA of mitochondrial genes in cultured mouse cortical neurons is referred to here as "DNAscope" as the probes target the mitochondrial DNA instead of RNA transcripts. Electroporated layer 2/3 pyramidal neurons were plated on 35 mm MatTek Dishes, cultured for either 14 or 21 days, and fixed in 4% paraformaldehyde for 15 minutes, followed by three 5 minute washes with PBS. The MatTek coverslips were detached from their culture dishes and the attached fixed cells were then treated with RNAscope® Hydrogen Peroxide Reagent for ten minutes at 23°C to 25°C and washed twice with deionized water, followed by digestion in a 1:15 dilution of RNAscope® Protease III Reagent in PBS at 23°C to 25°C and two washes in PBS. These steps constitute the pretreatment steps for fixed cell culture samples. EtOH dehydration was not used as this step would damage the critical fluorescent protein that labeled mitochondria in electroporated neurons. The first modification to the RNAscope Protocol involved inclusion of an incubation step with RNAse cocktail (RNase A at 20 U/mL; RNase T1 at 800 U/mL; Fisher Scientific) in Phosphate-buffered saline (PBS; Gibco™ 10010049) for 30 minutes at 37°C inside a HybEZ hybridization oven (ACD) immediately following the RNAscope hydrogen peroxide and protease pretreatment steps for fixed cell culture samples. Sample coverslips were rinsed twice in PBS and then incubated with pre-warmed target probes (20 nmol/L of each oligo probe) overnight. CY-B was targeted with RNAscope® Probe- Mm-mt-Cytb (ACD;Cat No. 517301), and CO1 was targeted with RNAscope® Probe- Mm-mt-Co1-C2 (ACD;Cat No. 517121-C2). The second modification to the RNAscope protocol involved extending the primary target probe incubation step to overnight (18-21 hours) at 40°C instead of 2 hours at 40°C inside the HybEZ hybridization oven (ACD). These two modifications have been previously implemented for targeting viral DNA (*57*). The option of a 60°C DNA denaturation step previously used for targeting viral DNA (*57*) was excluded as it would also denature the critical fluorescent protein that labeled mitochondria in electroporated neurons. After the overnight target

probe hybridization, the samples were incubated at 40°C in Amplifier 1 (preamplifier) (2 nmol/L) in hybridization buffer B (20% formamide, 5× SSC, 0.3% lithium dodecyl sulfate, 10% dextran sulfate, blocking reagents) for 30 minutes; Amplifier 2 (2 nmol/L) in hybridization buffer B at 40°C for 15 minutes; and Amplifier 3 (label probe) (2 nmol/L) in hybridization buffer C (5× SSC, 0.3% lithium dodecyl sulfate, blocking reagents) for 15 minutes. After each hybridization step, slides were washed with wash buffer (0.1× SSC, 0.03% lithium dodecyl sulfate) two times at room temperature (*58*). Chromogenic detection was performed utilizing a horseradish peroxidase (HPR) construct specific to each gene-dedicated imaging channel and a fluorescent Opal reagent of choice. CY-B was stained with Opal 520 Reagent (Perkin Elmer, FP1487001KT), and CO1 was stained with Opal 570 Reagent (Perkin Elmer, FP1488001KT). Each Opal reagent dye was diluted 1:1500 in RNAscope® Multiplex TSA Buffer. Coverslips were mounted onto slides in Fluoro-Gel (EMS; 17985-10) and analyzed at 60x magnification using a Nikon A1 confocal microscope.

Funding:

JSPS KAKENHI Grant Numbers JP19H03221 (YH), JP22H02716 (YH), JP22K18939 (YT), and JP22KJ1098 (YD)

AMED Grant numbers JP19dm0207082 (YH), JP21wm0525015 (YH, YT)

JST, PRESTO Grant Number JPMJPR16F7 (YH) and JPMJPR14FA (YT)

National Institute of Health- National Institute of Neurological Disorders and Stroke- R35 NS127232 (FP)

JST, FOREST Grand Number JPMJFR203K (YT)

Human Frontier Science Program (HFSP) (RGP0028/2022) (YT)

National Institute of Health- National Institute of General Medical Sciences – R35 GM137921 (TL)

ERC-CoG Inspire (IT, GC, JA)

The Leona M. & Harry B. Helmsley Charitable Trust (1903-03788) (JG)

NIH NCI 1DP2CA281605-01 (JG)

Author contributions:

Conceptualization: FP, TLL, YH

Methodology: YH, TLL, YD, DMV, AMD, GC, JA, YT, JTG, IT

Investigation: YH, TLL, YD, DMV, AMD, SH, GC, JA, MP, PK

Visualization: YH, TLL, YD, DMV, AMD, GC, PK, YT, JTG, IT, FP

Funding acquisition: YH, TLL, YT, JLG, IT, FP

Project administration: YH, TLL, FP

Supervision: TLL, YH, JTG, IT, FP

Writing – original draft: TLL, YH, FP

Writing – review & editing: YH, TLL, YD, DMV, AMD, GC, PK, YT, JTG, IT, FP

Competing interests: Authors declare that they have no competing interests.

Data and materials availability: All data are available in the main text or the supplementary materials.

Supplementary Materials

Figs. S1 to S4

References (*1-39)*

Movies S1

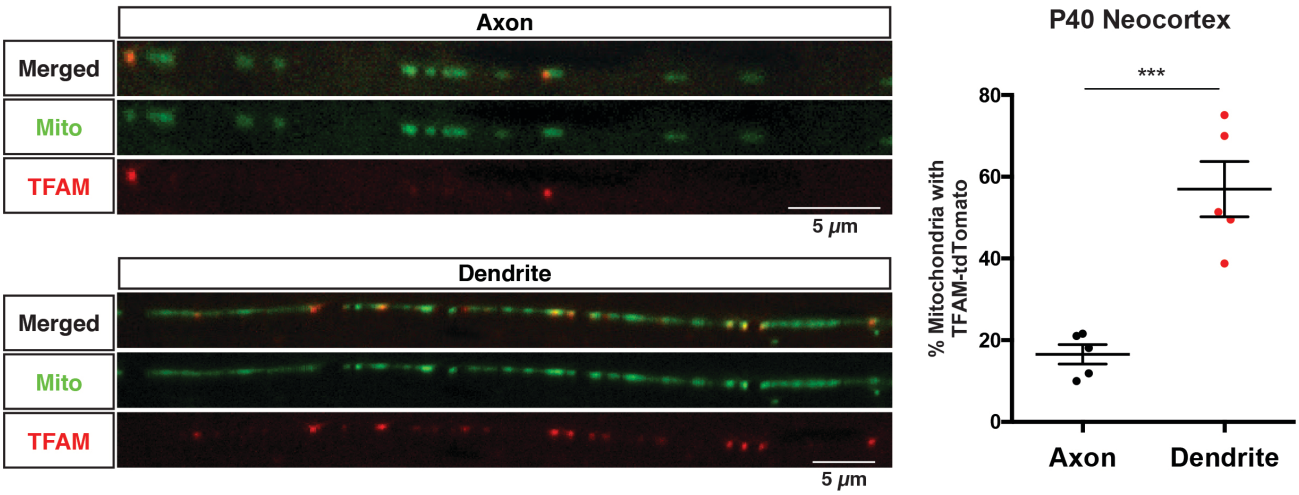

Supplemental Figure 1: A low fraction of axonal mitochondria contain mtDNA-associated protein TFAM compared to dendritic mitochondria *in vivo*. Related to Figure 1.

(**A-B**) Representative images of the axon (A) and a dendrite (B) of a layer 2/3 CPNs *in vivo* expressing TFAM-tdTomato and IMM-targeted mt-YFP at P40. Scale bar: 5μm. (**C**) Percentage of mitochondria positive for TFAM in the axon or dendrites. Numbers of mitochondria counted are shown in each column. 5 neurons from 2 mice at P40 and P69 were used for quantifications. *** p=0.0004 by paired t-test.

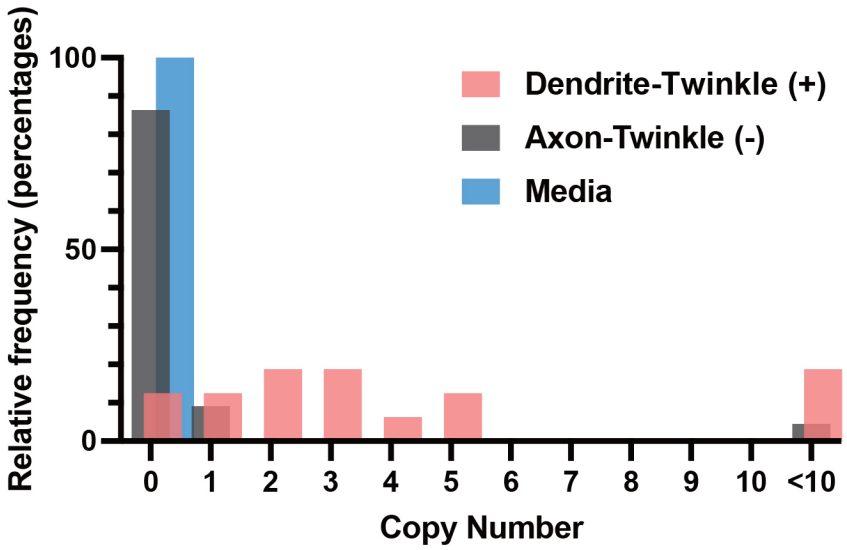

Supplemental Figure 2: mtDNA copy number distribution. Related to Figure 3

Relative frequency histograms of the copy number of mtDNA determine by qPCR for each isolated mitochondrion with Twinkle from dendrites (black), the isolated mitochondria without Twinkle from axons (red), and the culture media (blue; negative control).

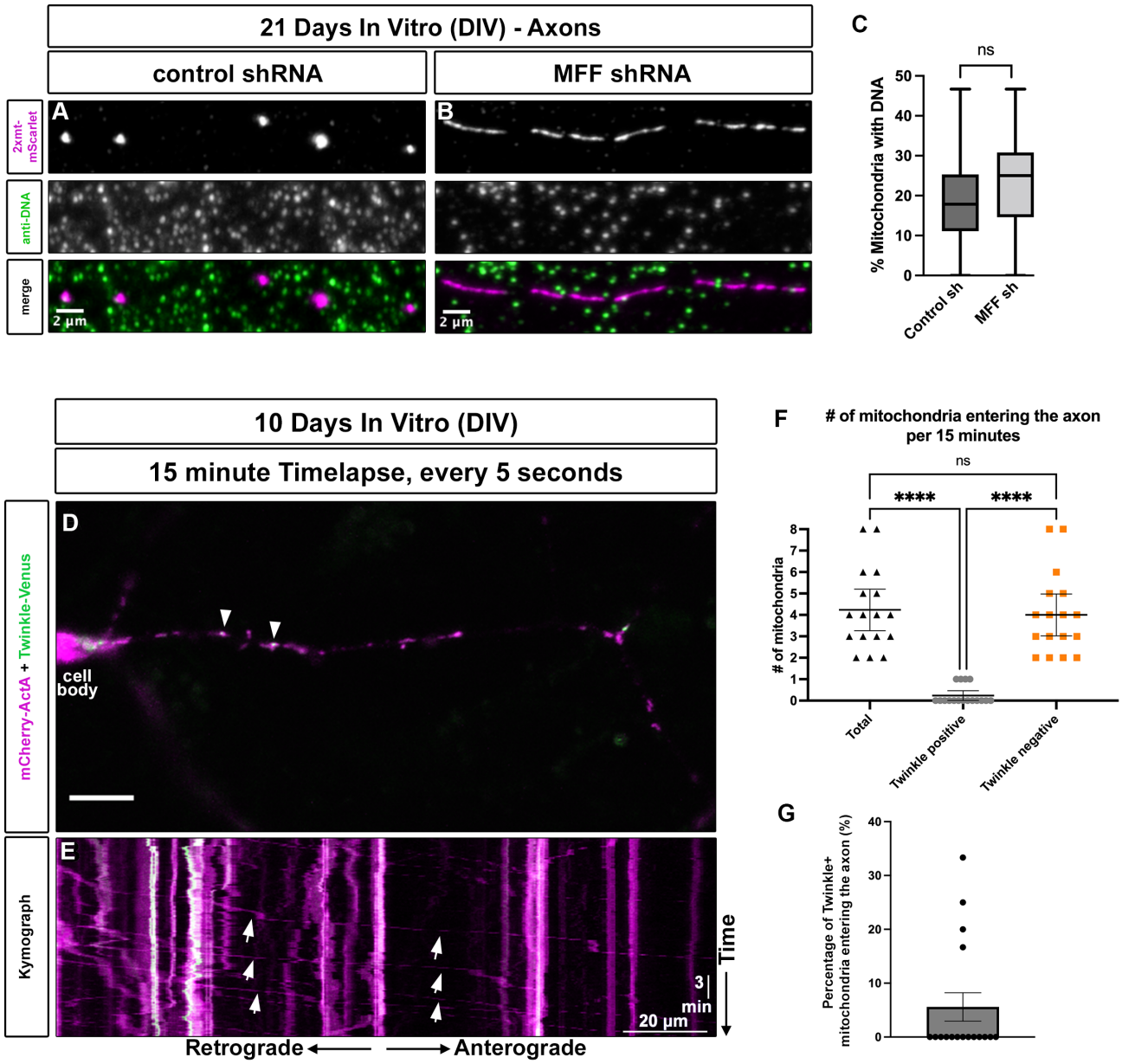

Supplemental Figure 3: Fraction of mtDNA+ mitochondria in axons is independent of fission and determined as they enter the axon. Related to Figure 3.

(**A-B**) Axonal mitochondria in CPNs electroporated with control shRNA are punctate and mostly lack DNA labeling (A). Blocking of mitochondrial fission using shRNA-mediated knockdown of Mff (B), elongates axonal mitochondria but does not impact DNA positivity, arguing that the coupling of mitochondrial fission to mtDNA replication is not a major mechanism for regulating mtDNA levels in the axon. (**C**) Quantification of the percentage of axonal mitochondria containing DNA following knockdown with the indicated constructs. $N_{control\ shRNA}$ = 335 mitochondria from 18 axon segments from 3 independent

cultures. $N_{Mff\ shRNA}$ = 314 mitochondria from 18 axon segments from 3 independent cultures. Graphs are minimum to maximum box plots with 25th, 50th, and 75th percentiles marked. ns = not significant by Brown-Forsythe and Welch ANOVA. (**D**) Representative image of a cell body and emerging axon of a CPN in culture (DIV10) labeled with mCherry-ActA (mitochondria) and a mtDNA-associated protein (Twinkle-Venus). (**E**) Kymograph of the axon shown in A, imaged every five seconds for fifteen minutes. (**F**) Quantification of the number of mitochondria entering the axon (left: total mitochondria), (middle: mitochondria from total with Twinkle labeling), (right: mitochondria from total without Twinkle labeling). (**G**) Quantification of the percentage of mitochondria entering the axon with Twinkle-Venus labeling, demonstrating that the majority of mitochondria entering the axon already lack markers of a nucleoid. n = 71 mitochondria from 17 axons from 3 independent cultures, ns = not significant, ****$p \leq 0.0001$ by Kruskal-Wallis test.

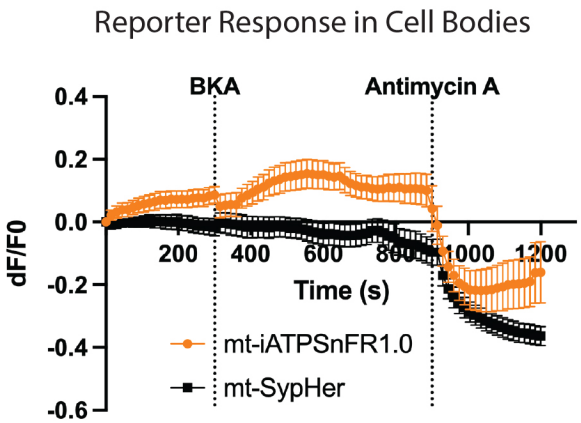

Supplemental Figure 4: BKA treatment does not significantly alter mitochondrial pH. Related to Figure 4.

The soma of cortical pyramidal neurons expressing either mt-iATPSnFR1.0 (orange) or mt-SypHer (black) were timelapse imaged for 20 minutes. At 5 minutes, bath application of bongkrekic acid (BKA, an inhibitor of the ATP transporter- adenine nucleotide translocase (ANT)) at 50µM was added and fluorescence intensity of the fluorescent reporter was monitored until 15 minutes, when Antimycin A at 1.25µM was added. As expected, in the cell body (just like in dendritic mitochondria- see Figure 4), BKA addition caused an increase in mt-iATPSnFR1.0 fluorescence over the next five minutes, followed by a dramatic decrease in mt-iATPSnFR1.0 fluorescence following Antimycin A. No observable difference in mt-SypHer fluorescence was observed for the 10 minutes following BKA addition, while a decrease was observed following Antimycin A addition. This argues that the increase observed in iATPSnFR1.0 is a result of ATP increase in the matrix and not a change in pH, while most of the effect observed following Antimycin A is a result of matrix acidification. $N_{mt\text{-}iATPSnFR1.0} = 10$ neurons from 3 independent cultures. $N_{mt\text{-}SypHer} = 10$ neurons from 3 independent cultures.

Supplemental Movie 1

Isolation of a single axonal mitochondrion using a nanopipette from the culture for 7DIV. Scale bar: 5 µm.